Reflection and Transmission of Oblique Acoustic Waves by a Sub-Critical Elastic Barrier with Discontinuities Using Analytical Numerical Matching

by

Mauricio Villa

Department of Mechanical Engineering and Materials
Duke University

Date: _____

Approved:

_____
Donald B. Bliss, Supervisor

_____
Linda Franzoni

_____
Earl Dowell

_____
Thomas Witelski

Thesis submitted in partial fulfillment of the requirements for the degree of
Master of Science in the Department of Mechanical Engineering and Materials
Science in the Graduate School of Duke University
2017

Abstract

Reflection and Transmission of Oblique Acoustic Waves by a Sub-Critical Elastic Barrier with Discontinuities Using Analytical Numerical Matching

by

Mauricio Villa

Department of Mechanical Engineering and Materials
Duke University

Date: _____

Approved:

_____
Donald B. Bliss, Supervisor

_____
Linda Franzoni

_____
Earl Dowell

_____
Thomas Witelski

An abstract of a thesis submitted in partial fulfillment of the requirements for the degree of Master of Science in the Department of Mechanical Engineering and Materials Science in the Graduate School of Duke University
2017

Abstract

This work develops models for the coupled structural-acoustic vibration of boundaries that reflect and transmit sound. First, the case of an infinitely long, fluid-loaded, sub-critical membrane that is periodically fixed and forced by oblique incident acoustic waves is considered. The method of Analytical Numerical Matching (ANM) is extended to deal with the resulting spatially-periodic and discrete phase-shifted forcing. The high resolution content of the solution near the constraints is analytically treated with a polynomial known as the Local Solution. The remaining, rapidly converging, part of the solution is treated modally and is known as the Global Solution. The Composite ANM Solution is then determined for the motion of the structure, and the far-field acoustic fields can be efficiently described. It is shown that the use of ANM effectively addresses the sensitivity of the acoustic fields and structure motion to the accuracy of which the local region near the structural discontinuities is resolved. The use of ANM is extended to demonstrate a method to deal with the mathematical difficulty of acoustic coincidence. The second module of this thesis presents ongoing work on the development of a model for a fluid-loaded finite membrane in an infinite baffle. Corrections to the in-vacuo structural wavenumber are developed to model the additional inertance and dissipative effects of the surrounding fluid media. The resulting dissipated energy as a function of frequency of the modified finite membrane is compared to energy radiated by the infinite, periodically driven, fluid loaded membrane to motivate further refinements of the finite model.

Contents

List of Figures

List of Symbols

Parameters with the subscript $(\ )_1$ correspond to the fluid medium above the structure, and $(\ )_2$ correspond to the fluid medium below the structure. Dimensional parameters are presented to define the non-dimensional parameters used throughout this work.

Dimensional Fluid and Structure Parameters

ρ_1, ρ_2	fluid density
c_1, c_2	fluid wave speed
ω	angular frequency
L	distance between structural constraints, length of bay
T	membrane tension
c_m	in-vacuo membrane wave speed
ρ_m	membrane linear density
i	imaginary number $i = \sqrt{-1}$
$\mathbb{Z}$	set of all integers

Non-dimensional Parameters

The characteristic length scale used throughout the non-dimensional scheme is the distance between constraints L, unless noted otherwise.

$\varepsilon_1, \varepsilon_2$	fluid loading ratio

$$\varepsilon_1 = \frac{\rho_1 L}{\rho_m}, \quad \varepsilon_2 = \frac{\rho_2 L}{\rho_m}$$

k_1, k_2 fluid wavenumber

$$k_1 = \frac{\omega L}{c_1}, \quad k_2 = \frac{\omega L}{c_2}$$

k_M in-vacuo structural wavenumber

$$k_M = \frac{\omega L}{c_m}$$

M_1, M_2 Mach number of in-vacuo structural wave

$$M_1 = \frac{k_1}{k_M}, \quad M_2 = \frac{k_2}{k_M}$$

z_1, z_2 acoustic impedance

$$z_1 = \frac{\varepsilon_1}{M_1} = \frac{\rho_1 c_1}{\rho_m c_m / L}$$
$$z_2 = \frac{\varepsilon_2}{M_2} = \frac{\rho_2 c_2}{\rho_m c_m / L}$$

P_I incident pressure amplitude

P_R reflected pressure amplitude

P_T transmitted pressure amplitude

p_s surface pressure on structure

F_a applied forcing

R reflection coefficient

T transmission coefficient

θ_i angle of incidence

θ_t primary angle of transmission

θ_r primary angle of reflection

k_{x1}, k_{x2} fluid wavenumber x-component

k_{y1}, k_{y2} fluid wavenumber y-component

L_1, L_2 linear operators

k_s forced structural wave wavenumber

η_{local} Local solution displacement

$\hat{\eta}_{local}$ Modified Local solution displacement

$\hat{\eta}_l$ Modified Local solution displacement on left of drive point

$\hat{\eta}_r$ Modified Local solution displacement on right of drive point

$\bar{\eta}_{local}$	Rescaled Local solution displacement
L_s	smoothing length
m	mode number
m_*	coincident mode number
$k_{x,m}$	modal description of x-component wavenumber
λ	scaling parameter
p_{D1}, p_{D2}	pressures from Driven Membrane
$p_{D1,Rad}, p_{D2,Rad}$	radiating pressures from Driven Membrane
$P_{D1,m}, P_{D2,m}$	scaled amplitude of radiating pressures from Driven Membrane
p_1, p_2	far-field pressures from Complete Problem
$\theta_{1,m}, \theta_{2,m}$	scattering angles from Driven Membrane
m_{Rad1}, m_{Rad2}	propagating modes
I_1, I_2	acoustic intensity
k_c	center frequency
η_{ff_1}	membrane displacement due to driven-fixed configuration
η_{ff_2}	membrane displacement due to fixed-driven configuration
$\left\langle \bar{V} \right\rangle_x^2$	spatially averaged mean-square velocity
k_M^*	resonant in-vacuo structural wavenumbers
$k_{-\delta}, k_{+\delta}$	lower and upper half-power frequencies
δ	frequency perturbation
$\bar{R}$	strength of damper suspension per unit length
γ	structural wavenumber for membrane on a viscous suspension
$\mathbb{P}$	power
k_{χ_i}	inertance correction for structural wavenumber, iteration i
$\tilde{M}_1, \tilde{M}_2$	effective Mach number of structural wave

Acknowledgements

The author would like to acknowledge his advisor, Dr. Donald B. Bliss, for his unrelenting mentorship and encouragement. Additionally, the support and assistance of The GEM Consortium, Fermi National Accelerator Laboratory, the Acoustical Society of America, and the E. Bayard Halsted Scholarship, is greatly appreciated.

And of course, gracias Mami y Papi.

1

Introduction

The motivation for this work is the need to predict sound fields and their spatial variation, as well as the need to reduce sound pressure levels, in architectural spaces and in aircraft and automobiles. The present work involves the derivation of more realistic acoustic reflection and transmission of models for flexible boundaries with structural discontinuities, such as ribs or braces. The first model developed is that of an infinitely long elastic membrane with periodic fixed line constraints that is forced with an oblique planar acoustic wave. Introducing the structural discontinuities redistributes the structural wavenumber spectrum to a finite set of radiating modes, as compared to the unconstrained membrane [2, p.76]. This problem can be solved using a modal series, termed in this thesis as the Classical Solution. However, the method of Analytical Numerical Matching (ANM) is applied to efficiently model the slowly converging regions near the structural discontinuities and reduce the computational requirements. The second part of this thesis explores the development of the structural-acoustic response of a finite elastic membrane with fixed endpoints placed in an infinite baffle, and forced with an oblique acoustic wave. This geometry serves as a model for one bay (the membrane segment between two consecutive constraints)

of the infinitely periodic structure.

Analytical/Numerical Matching is a general method originally developed by Dr. Donald Bliss, and has been applied to problems in vortex dynamics, rotorcraft free wake analysis, and structural acoustics [3, 4, 5]. The method has been applied to structural-acoustics problems such as an infinite membrane with normal acoustic forcing and structural discontinuities [1], and radiating cylindrical structures with structural discontinuities [6]. The method of ANM consists of separating the problem into a Global Solution, which is treated numerically, and a Local Solution, which treats the most rapidly varying parts of the system analytically. The analytical treatment of the local high resolution content, which in the current problem is associated with the structural discontinuities, allows for improved computational efficiency since it is expressed in closed form.

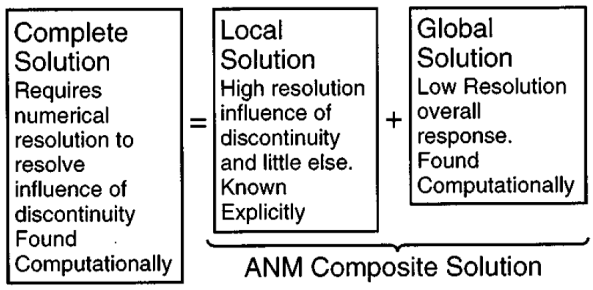

FIGURE 1.1: Summary of ANM Components [1]

The motivation to apply the method of ANM to the configuration in this thesis comes from the realization that near the location of the structural discontinuities, there is a small region with rapid spatial variation that would require high resolution to describe accurately, and this in turn results in greater computational effort than is otherwise needed by the overall system. Additionally, it is demonstrated that failure to accurately characterize the small region around the discontinuity can result in significant error throughout the system, when determining the acoustic scattering [1].

ANM directly addresses the issue of the high resolution content near the discontinuity by prescribing a solution in the form of a polynomial with defined characteristics. Once the Local Solution is determined, the smoothed distributed load required to create this motion is calculated using the structural equations. Finally, the overall system response, described by the Global Solution, is found with conventional modal methods, with the original discrete load replaced by the smoothed distribution used to satisfy the Local Solution. Finally, the Local and Global Solutions are superimposed to find the Composite ANM Solution.

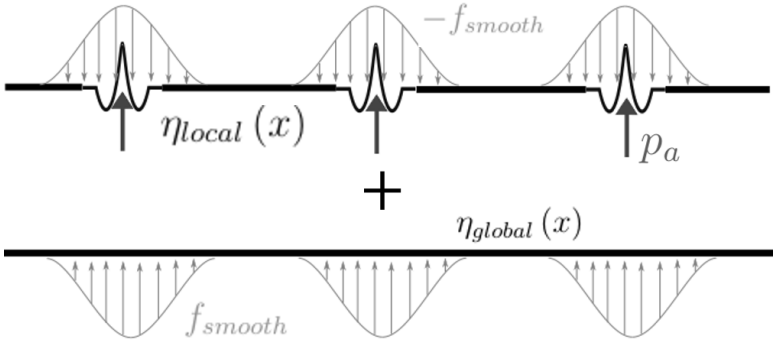

FIGURE 1.2: The Local Solution (Top) is forced by a discrete load p_a that is replaced by a smoothed forcing. The calculated smoothed forcing is applied to a small region and serves as the coupling to the Global Solution (Bottom)

In order to implement the ANM methodology, an intermediate length L_s, termed the smoothing length, is introduced. The smoothing length contains the entirety of the Local Solution and is therefore its largest length scale. It also appears in the Global Solution as one of the smaller length scales, and defines the region over which the two components overlap. Although the intermediate steps in formulating the Local and Global Solutions are dependent on the smoothing length, the final result is independent of the chosen smoothing length.

1.1 The Periodically Fixed Infinite Membrane

The first configuration considered in this thesis is the response of a fluid-loaded membrane with structural discontinuities that is acoustically driven with an oblique incident wave. The membrane is bounded on either side by two possibly distinct fluids with different fluid densities and acoustic wave speeds. The structural discontinuities are manifested by requiring that the membrane be periodically fixed, and therefore have zero displacement at these locations.

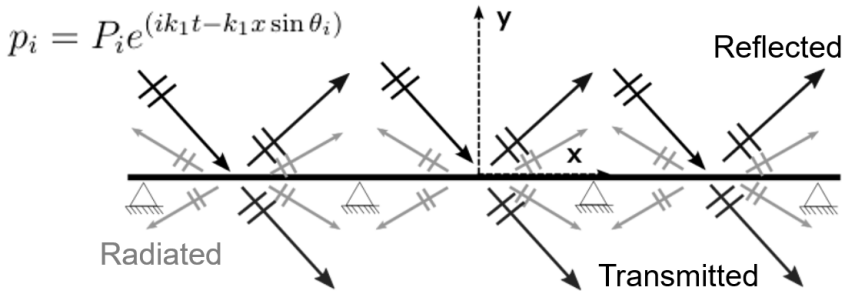

FIGURE 1.3: The Periodically Fixed Membrane is forced by an acoustic wave, and will result in a reflected and transmitted wave, as well as radiated (or scattered) waves due to structural reverberation

The problem posed is an important case study of structural-acoustic coupling and many different configurations of the fluid-loaded membrane have been studied. Morse and Ingard [7, p.622] treated a more general case of this configuration with regularly spaced impedance loads using a Green's Function formulation. Most recently, the case of a periodically fixed membrane acoustically driven with an incident wave normal to the membrane was treated by Loftman [1] with the method of ANM to describe the displacement of the membrane.

1.1.1 Decomposition into Unconstrained and Driven Membrane

The approach taken to model this problem is to resolve it into two manageable sub-problems. The response of the membrane, and its coupled fluid pressures, are

separated into two parts. The first sub-problem, termed the "Unconstrained Membrane", determines the dynamics due to the response of the free infinite membrane with fluid loading to the oblique incident wave. The second sub-problem, termed the "Driven Membrane", considers the dynamics due to the response of the fluid-loaded infinite membrane to the force influence of the discontinuities. This decomposition allows for the effect of the structural discontinuities to be isolated and understood. The solutions for these two sub-problems are developed in Chapters 2 and 3.

Once the solutions for these two sub-problems are determined, they are superimposed to build the response of the periodically fixed infinite membrane, which will be hence-forth refereed to as the "Periodically Fixed Membrane" for convenience. In order to correctly superimpose these sub-problems, the response of the Driven Membrane η_d is scaled to make the displacement at the constraint locations equal and opposite to that of the Unconstrained Membrane η_{free}. This scaling enforces that the net motion at the constraint locations is brought to rest. This scaling is represented mathematically as

$$\eta_{total} = \eta_{free} - \lambda \cdot \eta_d \tag{1.1}$$

given that there is a constraint at the origin, and the scaling factor λ is written in terms of the displacement at the drive-point. A similar scaling will be performed to describe the far-field acoustic behaviors coupled to the motion of the structure described by the Periodically Fixed Membrane.

1.2 The Baffled Finite Structure

The second configuration considered in this thesis is the response of a baffled finite elastic membrane that is fixed at the endpoints, and is forced with an oblique acoustic wave. Fahy [2, p.224] approached a similar problem, with a baffled plate, by expressing the transverse velocity of the structure as a summation over the in-vacuo

modes and then applied a Fourier transform to determine the radiated field.

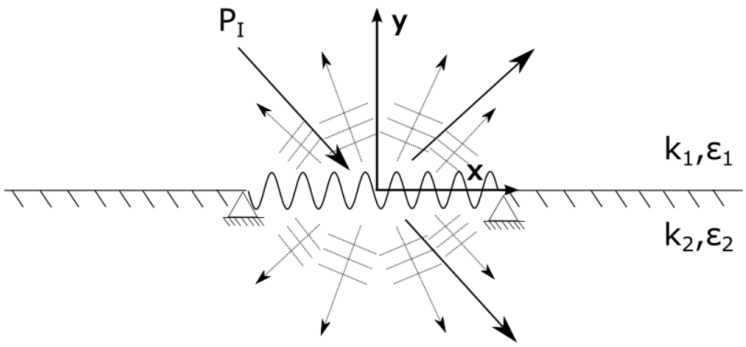

FIGURE 1.4: The Finite Membrane is forced by an acoustic wave and will result in radiated (or scattered) waves into both fluid media, with significant energy content in the primary angles of reflection and transmission

This model is also developed by linearly separating it into two simpler sub-problems: the response of a segment of the Unconstrained Membrane (as previously defined), and the scaled response of a finite membrane driven at the end-points. The amplitude and phase of the prescribed displacement at the end-points of the discretely driven component are scaled to the end-point displacement of the Unconstrained Membrane segment to bring the net displacement to zero. The response of the segment from the unconstrained motion is solved with the fluid back-loading from both media. For the end-driven component of the solution, the in-vacuo response of the structure is first considered. The influence of the fluids is introduced to the end-driven model by developing inertance and damping approximations for the structure motion.

2

Unconstrained Infinite Membrane

The motion of an acoustically driven, fluid-loaded infinite membrane is first considered in order to present the simplest building block of the two problems investigated in this thesis. The acoustic forcing is in the form of an obliquely incident acoustic plane wave that is harmonic in time. The analysis of the Unconstrained Membrane bounded by distinct fluids is considered using two slightly different conceptual interpretations. The first approach simultaneously solves the fully coupled structural and acoustic equations of motion. The second approach resolves the problem into the resultant acoustic field due to a "hard-wall reflection" from the barrier and the corresponding radiation problem due to the dynamics of the barrier. In the next section the governing equations are described. The response of the membrane and acoustic fields is calculated by solving the governing equation of the membrane, applying the boundary condition of continuous normal velocity at the membrane interface, and requiring that there be only waves propagating away from the membrane and exponential decay of evanescent waves far away from the membrane. All quantities and parameters are non-dimensional.

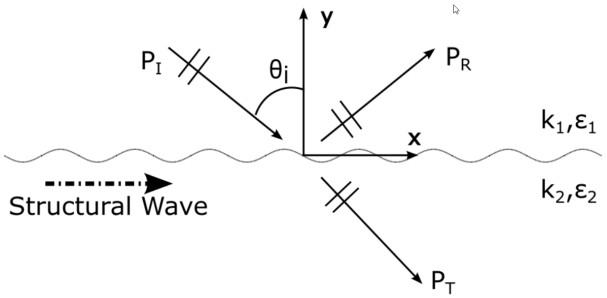

FIGURE 2.1: Unconstrained Membrane problem statement

2.1 Mathematical Formulation

2.1.1 Acoustic Fields

For the two fluids, the acoustic wave equation is the governing equation of the mediums. Because the problem is time harmonic, it reduces to the Helmholtz equation [8, p.93]

$$\left(\nabla^2 + k_i^2\right) p_{f,i} = 0 \tag{2.1}$$

where the subscript i refers to either the top fluid (i=1,$y > 0$) or the bottom fluid (i=2, $y < 0$), and k_i is the non-dimensional wavenumber of the fluid. As previously stated, the problem consists of an incident wave p_I with an incidence angle of θ_i from the normal to the membrane. The solutions to the wave equations physically describe an outgoing reflected pressure wave p_R in the top fluid and a transmitted wave p_T in the bottom fluid. The forms of these waves are presented below cite[p.195]Blackstock.

$$p_I = P_I e^{i(k_1 t - k_{x1} x + k_{y1} y)} \tag{2.2}$$

$$p_R = P_R e^{i(k_1 t - k_{x1} x - k_{y1} y)} \tag{2.3}$$

$$p_T = P_T e^{i(k_1 t - k_{x2} x + k_{y2} y)} \tag{2.4}$$

The components of the top fluid wavenumber are geometrically defined using the incidence angle of the incoming pressure wave to be

$$k_{x1} = k_1 \sin\theta_i \quad \text{and} \quad k_{y1} = k_1 \cos\theta_i \tag{2.5a}$$

This system exhibits the well known behavior of specular reflection; that is that the reflected angle is equal to the incidence angle $\theta_R = \theta_i$ [8, p.143]. The wavenumber components of the bottom fluid are similarly found by the relationships

$$k_{x2} = k_2 \sin\theta_t \quad \text{and} \quad k_{y2} = k_2 \cos\theta_t \tag{2.5b}$$

In order to determine the angle of transmission θ_t into the bottom fluid, it is necessary to recognize that the wavenumber in the x-direction must be continuous at the boundary ($y = 0$) for all x, so that

$$k_{x1} = k_{x2} \tag{2.6}$$

and therefore the angle of transmission into the bottom fluid θ_t is defined as

$$\cos\theta_t = -i\sqrt{\left(\frac{k_1}{k_2}\sin\theta_i\right)^2 - 1} \tag{2.7}$$

which is a representation of Snell's Law [9, p.188]. It is interesting to note that for this configuration, there is at most only one angle of reflection and one angle of transmission for a given incidence angle and given acoustic wavenumbers. The pressure amplitudes of the reflected and transmitted waves are determined by satisfying the boundary condition of continuous normal velocity at the structure surface ($y = 0$ plane). The velocity field of each fluid medium is related to the pressure description using the momentum equation [10, p.11]. The vertical component V_i of the velocity field is determined by

$$ik_i V_i = -\frac{M_i}{\varepsilon_i}\frac{\partial p_i}{\partial y} \tag{2.8}$$

The non-dimensional parameters M_i and ε_i compare the properties of the fluid to the structural properties of the membrane. The parameter M_i is a Mach number that compares the in-vacuo wave speed of the membrane to the speed of sound in

the fluid of interest. The parameter ε_i is a non-dimensional fluid-loading parameter that compares the characteristic fluid density to the linear density of the membrane. The governing equations of the membrane are introduced next.

2.1.2 Structural Dynamics

An infinitely long membrane is located at the $y = 0$ plane, separating the two fluid domains. Balancing the forces on the membrane yields the governing equation below for the transverse displacement of the membrane [11, p.10]. The pressure term on the right-hand side represents the total surface pressure on the membrane from the hydrodynamic and radiation loading from both fluids[1] and the parameter c_m denotes the in-vacuo structural wave speed of the membrane defined in terms of the tension and linear density of the structure.

$$\nabla^2 y - \frac{1}{c_m^2}\frac{\partial^2 y}{\partial t^2} = -\bar{p}_s(x, z, t) \tag{2.9a}$$

$$c_m = \sqrt{\frac{T}{\rho_m}} \tag{2.9b}$$

Rewriting this expression in non-dimensional form and recognizing that there is no variation in the z-coordinate due to the geometry of the problem, the transverse displacement of the membrane $\eta(x, t)$ is governed by the one-dimensional equation

$$-\frac{\partial^2 \eta}{\partial x^2} - k_M^2 \eta = -p_s(x, t) \tag{2.10a}$$

$$k_M = \frac{k_1}{M_1} = \frac{k_2}{M_2} \tag{2.10b}$$

where the time-harmonic properties of the problem have been used to further simplify the governing equation. The parameter k_M is the non-dimensional in-vacuo

[1] The bar over the $\bar{p}_s$ is notation meant to differentiate this pressure term from the non-dimensional pressures used throughout this work.

wavenumber of the membrane and can be written in terms of the Mach number of either fluid. The time harmonic term $e^{ik_1 t}$ will be assumed to apply to all motions and subsequently will not be explicitly written.

2.2 Method 1: Complete Fluid Loaded Problem

The first approach to solving for the motion of the membrane and pressure fields is done by recognizing that the total pressure on the surface of the structure $p_s(x)$ is a result of the incident, reflected, and transmitted pressure fields.

$$p_s(x) = (p_I + p_R - p_T)|_{y=0} = P_I e^{-ik_1 \sin\theta_i x}(1 + R - T) \tag{2.11}$$

with the reflection and transmission coefficients defined as $R = \frac{P_R}{P_I}$ and $T = \frac{P_T}{P_I}$, respectively. Thus, the structural dynamics of the membrane are coupled to the fluid dynamics. Assuming all transients have decayed, the displacement and velocity of the membrane are assumed to have a solution of the form

$$\eta = N e^{-ik_1 \sin\theta_i x} \tag{2.12a}$$

$$\frac{\partial \eta}{\partial t} = ik_1 N e^{-ik_1 \sin\theta_i x} \tag{2.12b}$$

Finally, in order to close the system of equations and identify a unique solution, the boundary condition of continuous vertical velocity at the boundary must be enforced.

$$\frac{\partial \eta}{\partial t} = V_1\Big|_{y=0} = i\frac{M_1}{\varepsilon_1 k_1}\frac{\partial(p_I + p_R)}{\partial y}\Big|_{y=0} \tag{2.13a}$$

$$\frac{\partial \eta}{\partial t} = V_2\Big|_{y=0} = i\frac{M_2}{\varepsilon_2 k_2}\frac{\partial p_T}{\partial y}\Big|_{y=0} \tag{2.13b}$$

There are three unknowns: the displacement of the membrane η, and the amplitudes of the reflected and transmitted pressure waves (or rather, the reflection and transmission coefficients R and T). Using the two boundary conditions in Eqn. 2.13 and

the governing equation of the membrane Eqn. 2.10a, the linear system of equations can be solved as

$$\eta = \frac{P_I(1+R-T)}{\left(\frac{k_1}{M_1}\right)^2 - (k_1 \sin\theta_i)^2} e^{-ik_1 \sin\theta_i x} \tag{2.14a}$$

$$R = \frac{iM_1\varepsilon_2 + M_2 \cos\theta_t \left(-i\varepsilon_1 \sec\theta_i + k_1\left(-1 + M_1^2 \sin^2\theta_i\right)\right)}{iM_1\varepsilon_2 + M_2 \cos\theta_t \left(i\varepsilon_1 \sec\theta_i + k_1\left(-1 + M_1^2 \sin^2\theta_i\right)\right)} \tag{2.14b}$$

$$T = \frac{2iM_1\varepsilon_2 \cos\theta_i \sec\theta_t}{iM_2\varepsilon_1 + \cos\theta_i \left(iM_1\varepsilon_2 \sec\theta_t + k_1 M_2\left(-1 + M_1^2 \sin^2\theta_i\right)\right)} \tag{2.14c}$$

The motion of the membrane and the pressure fields are simultaneously determined and found to be functions of the structural and fluid properties, as well as the amplitude and incidence angle of the incident pressure wave. These results will be briefly discussed after the second method of approaching this problem is considered.

2.3 Method 2: Hard Wall Reflection and Membrane Radiation

The second method of solving for the response of the Unconstrained Membrane introduces an intermediate step which prompts a physical understanding of the effect of the membrane on the reflected and transmitted pressure waves. The problem of the acoustically driven Unconstrained Membrane is recast as the superposition of the pressure field due to a rigid-boundary reflection, and the radiated pressure fields produced from the motion of the membrane resulting from the rigid-boundary surface force.

2.3.1 Hard Wall Reflection

The first component of this approach describes the resultant pressure field from a perfect reflection of the incident oblique pressure wave. It can be formally shown that by requiring the boundary condition at the $y = 0$ plane to be that of zero vertical

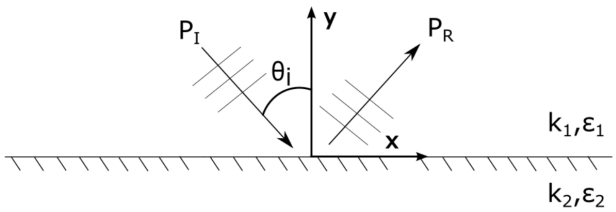

FIGURE 2.2: Hard wall reflection of incident acoustic wave problem statement

velocity (thereby, a rigid wall), then the reflected wave will have an equal amplitude to the incident pressure and the same angle of reflection.

$$V_1\Big|_{y=0} = 0 = i\frac{M_1}{\varepsilon_1 k_1}\frac{\partial(p_I + p_R)}{\partial y}\Big|_{y=0} \tag{2.15a}$$

requires that

$$P_I = P_R \tag{2.15b}$$

Similarly, as a result of the rigid-boundary boundary condition, there is no velocity (or energy) transferred into the bottom fluid domain and so the amplitude of the transmitted pressure is $P_T = 0$. Therefore, the surface pressure at the $x = 0$ plane is

$$p_s = (p_I + p_R)\Big|_{y=0} = 2P_I e^{-ik_1 \sin\theta_i x} \tag{2.16}$$

2.3.2 Membrane Radiation

The second component of this approach determines the radiated pressures from the membrane motion when forced by the surface pressure determined from the hard wall reflection.

Defining the external load acting on the membrane as the resultant surface pressure found from the rigid boundary condition case and the radiation loading, the equation of motion of the membrane (from Eqn. 2.10a) becomes

$$-\eta'' - \left(\frac{k_1}{M_1}\right)^2 \eta = -2P_I e^{-ik_1 \sin\theta_i x} - (p_{Rad1} - p_{Rad2})\Big|_{y=0} \tag{2.17}$$

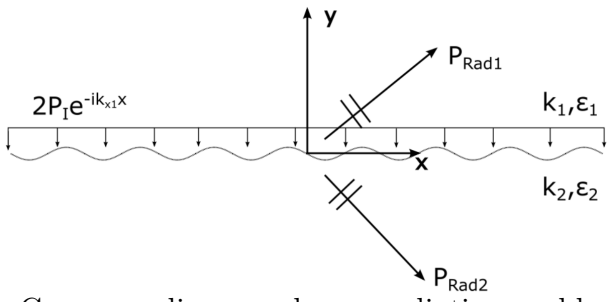

FIGURE 2.3: Corresponding membrane radiation problem statement

The fluid back loading on the structure p_{Rad} is a function of the motion of the membrane (Eqn. 2.12a), and is determined by relating the fluid pressures in both media to the vertical velocity components using the momentum equation and then enforcing the condition of continuous vertical velocity at the boundary. Therefore,

$$p_{Rad1} = i\frac{k_1\varepsilon_1}{M_1^2\cos\theta_i}Ne^{-ik_1\sin\theta_i x}e^{-ik_{y1}y} \tag{2.18a}$$

$$p_{Rad2} = -i\frac{k_1\varepsilon_2}{M_1^2\cos\theta_t}Ne^{-ik_1\sin\theta_i x}e^{ik_{y2}y} \tag{2.18b}$$

where p_{Rad1} and p_{Rad2} are the pressures radiated into the top and bottom fluids respectively. Finally, using these expressions for pressures and substituting into the membrane equation of motion, the displacement amplitude of the membrane is found to be

$$N = \frac{-2P_i}{\left(k_1\sin\theta_i\right)^2 - k_M^2 + \frac{ik_1\varepsilon_1}{M_1^2\cos\theta_i} + \frac{ik_1\varepsilon_2}{M_1^2\cos\theta_t}} \tag{2.19}$$

$$\eta = \frac{-2P_i}{\left(k_1\sin\theta_i\right)^2 - k_M^2 + \frac{ik_1\varepsilon_1}{M_1^2\cos\theta_i} + \frac{ik_1\varepsilon_2}{M_1^2\cos\theta_t}}e^{-ik_1\sin\theta_i x} \tag{2.20}$$

and so the motion of the membrane, and radiated pressures, are found to be functions of the incident pressure amplitude and angle, as well as the fluid and structural properties.

2.3.3 Assembled Pressure Fields

Applying linearity, the membrane motion and fluid pressures of both components just described Section 2.3 can be combined by superposition. The hard wall reflection does not effect the motion of the membrane that was determined in Eqn. 2.19, it only contributes to the resultant reflected and transmitted pressure fields so that

$$p_R = P_I \left(1 - \frac{i2k_1\varepsilon_1}{M_1^2 \cos\theta_i \left((k_1 \sin\theta_i)^2 - k_M^2 + \frac{ik_1\varepsilon_1}{M_1^2\cos\theta_i} + \frac{ik_1\varepsilon_2}{M_1^2\cos\theta_t} \right)} \right) e^{i(-k_1 \sin\theta_i x - {}_1 k_y y)} \tag{2.21a}$$

$$p_T = \frac{i2k_1\varepsilon_2 P_I}{M_1^2 \cos\theta_t \left((k_1 \sin\theta_i)^2 - k_M^2 + \frac{ik_1\varepsilon_1}{M_1^2\cos\theta_i} + \frac{ik_1\varepsilon_2}{M_1^2\cos\theta_t} \right)} e^{i(-k_1 \sin\theta_i x + {}_2 k_y y)} \tag{2.21b}$$

This approach has allowed for a solution that is particularly useful in interpreting the effect of the fluid back loading and structural properties. These behaviors are presented in the next section.

2.4 Analysis of Unconstrained Membrane

The membrane and fluid behaviors determined from the two approaches presented in this chapter are equivalent. Method 1 allows for a very systematic solution process-however understanding the results may be obscured by the mathematics. Although less direct, the "Membrane Radiation" decomposition allows for a clearer interpretation of the physical behavior of the system.

2.4.1 Membrane Behavior

The first characteristic of this system that is evident in both approaches is that for a given incident pressure wave there is only one structural wave on the membrane, with a wavenumber

$$k_s = k_{x1} = k_1 \sin\theta_i \tag{2.22}$$

Note that k_s is the wavenumber of the driven transverse wave on the membrane and a function of the driving frequency and incidence angle, while k_M is the in-vacuo wavenumber of the membrane and is a function of the inherent structural properties. Since this thesis focuses on sub-critical (or subsonic) membranes, the special case of acoustic coincidence of $M_1 = 1$ where $k_s = k_M$ is not considered for the Unconstrained Membrane.

The expression for the amplitude of the membrane displacement Eqn. 2.19 is particularly useful for seeing the effect that the fluid back-coupling has on the membrane motion. The fluid loading parameters ε_1 and ε_2 in the denominator suggest that as the fluid loading increases, the magnitude of membrane displacement tends to decrease and there is an accompanying change in phase. By setting the fluid loading parameters to zero, the in-vacuo motion of the driven unconstrained motion is determined. Introducing the fluid loading terms in the denominator can be interpreted, at least to first order, as a frequency-dependent damping and added inertance. This observation is motivated by the known mechanical impedance of a simple spring-mass-damper system $z = F/v = R + i(m\omega - s/\omega)$ [8, p.12], and will serve as motivation for fluid loading models in Chapter 5.

2.4.2 Acoustic Fields

As previously stated, the Unconstrained Membrane exhibits the behavior of specular reflection, where the reflection angle of the pressure wave is equal to the angle of the incident pressure wave. If the configuration did not include a fluid in the negative y half-space, there would be no medium for a transmitted wave and all of the energy would be reflected back into the positive y half-space. There is no energy dissipated by the membrane since there is no resistive element inherent to the structure. Instead the influence of the membrane would be to modify the phase of the reflected pressure wave as compared to the incident wave. The result in Eqn. 2.21 suggests that when

both fluid media are considered, the effect of the membrane is to not only change the phase of the reflected wave, but also reduce its amplitude so as to allow for the possibility of a transmitted wave.

In order to characterize the energy reflected and transmitted due to an incident pressure wave at a single frequency and angle, the acoustic intensity components normal to the structure are calculated for both fluids [8, p.125], [12, p.64]. The top fluid intensity occurs completely at the reflection angle. This simple reflection angle θ_R is termed the "primary angle of reflection", and will become significant when considering the Periodically Fixed Membrane. The magnitude of the intensity of the top fluid is dependent on the reflection coefficient R, which was defined in Eqn. 2.14b. The intensity in the bottom fluid occurs completely at the transmission angle θ_t, given that it is real valued, and would be proportional to the transmission coefficient T, the ratio of the (non-dimensional) fluid impedances. The angle of transmission θ_t will likewise be termed the "primary angle of transmission." The spatially averaged intensity distributions radiating away from the structure for both the top fluid I_1 and the bottom fluid I_2 are normalized to the spatially averaged incident intensity normal to the structure. These incident and outgoing intensities are defined as

$$I_{incident} = \frac{|P_I|^2 \cos\theta_i}{2 \cdot (\varepsilon_1 / M_1)} \tag{2.23a}$$

$$I_1 = |R|^2 \tag{2.23b}$$

$$I_2 = \frac{k_{y2}\ \varepsilon_1}{k_{y1}\ \varepsilon_2}|T|^2 \tag{2.23c}$$

If the membrane configuration investigated does not result in a real transmission angle, all of the incident energy is reflected back at the primary angle [8, p.157].

3

Periodically Driven Membrane

It is reasoned that the influence of the fixed constraint on the membrane can be modeled as an appropriately-scaled discrete line force acting on the structure [1]. The mathematical framework presented in Chapter 2 is used and extended to develop a solution for the membrane motion and resultant pressure fields of a periodically driven membrane using the method of Analytical Numerical Matching.

3.1 Problem Statement

The problem of interest in this chapter is depicted in Figure 3.1 below. The equally spaced vertical arrows represent the spatially periodic discrete line force F_a acting on the structure. Unlike in the Unconstrained Membrane, there is no incident pressure wave acting on the structure. The governing equation for the Driven Membrane motion is

$$-\frac{\partial^2 \eta_d}{\partial x^2} - k_M^2 \eta_d = F_a - p_s \tag{3.1}$$

where the functional forms of the discrete applied force F_a and the fluid back-loading p_s are defined next. For convenience, the linear operator L_1 will from hence forth be

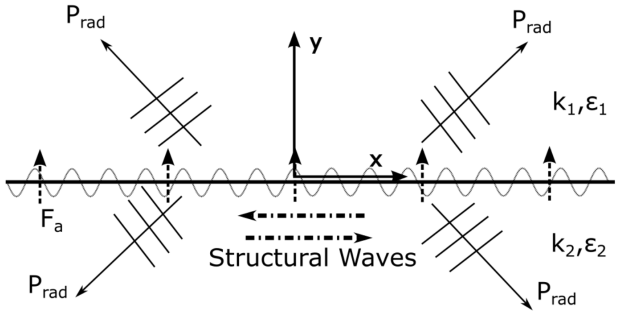

FIGURE 3.1: Periodically driven, fluid-loaded infinite membrane.

defined as

$$L_1[\,] \equiv -\frac{\partial^2}{\partial x^2}[\,] - k_M^2[\,] \tag{3.2}$$

3.1.1 Phase-Shifted Periodic Line Forcing

As described in Section 1.1.1, the displacement of the Driven Membrane η_d drive-points have to be equal and opposite to the corresponding displacements of the Unconstrained Membrane in order to bring the fully assembled motion (that of the Periodically Fixed Membrane) to rest at the constraint locations. This is accomplished by applying a discrete line force F_a on the membrane at the locations of the constraints of the form

$$F_a = f_o \sum_{n=-\infty}^{+\infty} \delta(x-n) \tag{3.3a}$$

which is a functional form known as an impulse train or Dirac Comb [13]. The amplitude of the forcing f_o is scaled to have the required magnitude to negate the unconstrained motion at the fixed locations. The delta function applies the force at a discrete line $x = n$. The distance between each bay is the characteristic length used in the non-dimensionalization scheme so that the locations of the discrete forces are at integer values along the x-axis. However, in order for the Dirac Comb forcing to be equal and opposite to the displacement of the Unconstrained Motion that is driven with an incident wave of oblique incidence, it is necessary to allow the components

of the Dirac Comb to be appropriately phase-shifted. This is accomplished by introducing a phase shift that is equivalent to the driven structural wave wavenumber $k_s = k_1 \sin\theta_i$ of the Unconstrained Membrane. Therefore, the periodic driving force on the membrane has the form

$$F_a = f_o \sum_{n=-\infty}^{+\infty} \delta(x-n)\, e^{-ik_1 \sin\theta_i x} \tag{3.3b}$$

which we define as phase-shifted Dirac Comb forcing of the driven membrane [14].

3.1.2 Fluid Back-Loading

The coupling of the fluid media to the motion of the structure is also included in the development of the governing equation of the membrane as a pressure acting on the surface p_s. This resultant membrane radiation follows the same development as that presented in Section 2.3.2, so that

$$p_{Rad1} = i\frac{k_1^2 \varepsilon_1}{M_1^2 k_{y1}} e^{-ik_{y1}y} \eta_d(x) \tag{3.4a}$$

$$p_{Rad2} = -i\frac{k_1^2 \varepsilon_2}{M_1^2 k_{y2}} e^{ik_{y2}y} \eta_d(x) \tag{3.4b}$$

and

$$p_s = (p_{Rad1} - p_{Rad2})\Big|_{y=0} \tag{3.4c}$$

The wavenumber components in the y-direction are rewritten as

$$k_{y1} = -i\sqrt{k_x^2 - k_1^2} \tag{3.5a}$$

$$k_{y2} = -i\sqrt{k_x^2 - k_2^2} \tag{3.5b}$$

where this form has been used to ensure that only waves propagating away from the structure are permitted and that all other waves exponentially decay as y increases.

These expressions will be subsequently used in describing the vertical component of the fluid wavenumbers.

3.1.3 Resultant Membrane Governing Equation

Using the expressions developed, the governing equation for the displacement of an infinite, fluid-loaded, membrane that is driven by a phase-shifted Dirac Comb line forcing is

$$L_1[\eta_d] = f_o \sum_{n=-\infty}^{+\infty} \delta(x-n)\, e^{-ik_1 \sin\theta_i x} + \left(\frac{k_1}{M_1}\right)^2 \left(\frac{\varepsilon_1}{\sqrt{k_x^2 - k_1^2}} + \frac{\varepsilon_2}{\sqrt{k_x^2 - k_2^2}}\right) \eta_d \quad (3.6)$$

The displacement of the driven membrane is solved using the method of Analytical Numerical Matching in order to efficiently treat the rapidly varying regions localized near the drive points.

3.2 Analytical Numerical Matching

The process of ANM carefully prescribes an analytical displacement η_{local} to a small region near each drive point that satisfies the structural discontinuity (the discrete line force), and determines the required external loading necessary to achieve this local displacement [1]. The prescribed Local Solution is chosen such that this required external loading, termed the "smoothed forcing" f_{smooth}, is a distributed load that quickly converges using traditional modal methods. The negative of this smoothed forcing is then applied to the Global Solution in order to cancel this introduced forcing.

$$L_1\left[\eta_d\right] = L_1\left[\eta_{global}\right] + L_1\left[\eta_{local}\right] = \left(F_a - f_{smooth} + f_{smooth}\right) - \left(p_s^{global} + p_s^{local}\right) \quad (3.7)$$

The terms can be grouped to demonstrate which loads are associated with the global and local problems.

$$L_1\left[\eta_d\right] = \overbrace{\left(f_{smooth}\left(x\right) - p_s^{global}\right)}^{\text{Global motion loads}} + \overbrace{\left(F_a - f_{smooth}\left(x\right) - p_s^{local}\right)}^{\text{Local motion loads}} \tag{3.8}$$

3.3 Local Problem

An intermediate length, termed the "smoothing length" L_s, is introduced in order to distinguish between the high resolution (Local Solution) and low resolution (Global Solution) regions. The Local Solution is designed such that it describes the rapidly varying motion near the drive point and the displacement outside the smoothing length is set to zero.

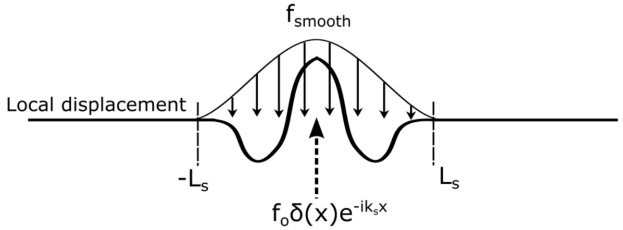

FIGURE 3.2: Local Solution and applied loads. The displacement inside the smoothing length is prescribed using a polynomial description, and outside this region it is set to zero.

3.3.1 Transferring the Fluid Pressures from the Local Solution

The governing equation for the Local Solution of the membrane is

$$L_1[\eta_{local}] = -\eta''_{local} - k_M^2\eta_{local} = f_o\delta\left(x-n\right)e^{-ik_1\sin\theta_i x} - f_{smooth} - p_s^{local} \tag{3.9}$$

which can be rearranged to solve for the smoothed loading below, where the terms labeled as $f_{structural}$ are the contributions to the smoothed loading from the structural dynamics.

$$f_{smooth} = \underbrace{-L_1[\eta_{local}] + f_o\delta(x-n)}_{f_{structural}} - p_s^{local} \tag{3.10}$$

However, it is important to recognize that the fluid pressures due to the motion of the Local Solution affect the entire length of the membrane. These fluid pressures serve as a non-structural mechanism to couple the local and global motions, and therefore are a global phenomenon. Reasoning that these fluid pressures will be smooth and continuous, since the membrane velocity in the Local Solution will be defined as such, the objective is to transfer these fluid pressures from the Local Solution into the Global Solution formulation so they can be treated modally.

Substituting the expression for the smoothed forcing Eqn. 3.10 and rearranging Eqn. 3.8, the pressures from the local motion are transferred to the global problem.

$$L_1\left[\eta_d\right] = \overbrace{\left(f_{structural}\left(x\right) - p_s^{local} - p_s^{global}\right)}^{L_1[\eta_{global}]=} + \overbrace{\left(F_a - f_{structural}\left(x\right)\right)}^{L_1[\eta_{local}]=} \tag{3.11}$$

The Local Solution can now be interpreted as being solved in-vacuo to determine the required forcing $f_{structural}$, and the resulting fluid pressures from the local motion are transferred to the global problem to be treated modally.

3.3.2 Modified Linear Operator for Oblique Incidence

For the Local Solution, the mechanical system is in essence being solved backwards since it is assumed that the displacement is known, and the required distributed load $f_{structural}$ is the unknown to be determined. Due to the phase-shifted Dirac Comb forcing, the phase of the Local Solution at each drive point must be treated carefully. The governing equation for the Local Solution displacement for the discrete force located at $x = n$ is reproduced below.

$$L_1[\eta_{local}] = -\eta''_{local} - k_m^2\eta_{local} = f_o\delta\left(x - n\right)e^{-ik_1\sin\theta_i x} - f_{structural} \tag{3.12}$$

Assuming that the local displacement will have a phase functional dependence like that of the line forcing, then the local displacement and smoothed force can be

rewritten as

$$\eta_{local}\left(x\right) = \hat{\eta}_{local}\left(x\right) e^{-ik_1 \sin\theta_i x} \tag{3.13a}$$

$$f_{structural}\left(x\right) = \hat{f}_{structural}\left(x\right) e^{-ik_1 \sin\theta_i x} \tag{3.13b}$$

This reformulation of the functions allows the exponential with the phase-shift information from each discrete applied force to be separated and canceled. By substituting these expressions into Eqn. 3.12, a new linear operator L_2 acting on the modified function $\hat{\eta}_{local}$ is defined [14] as

$$L_2[\hat{\eta}_{local}] \equiv -\hat{\eta}''_{local} + 2ik_1 \sin\theta_i \hat{\eta}'_{local} + \left((k_1 \sin\theta_i)^2 - k_M^2\right) \hat{\eta}_{local} \tag{3.14}$$

and applying the external loading,

$$L_2[\hat{\eta}_{local}] = f_o \delta(x-n) - \hat{f}_{structural} \tag{3.15}$$

If the Driven Problem being considered were chosen for the normal incidence configuration of the Periodically Fixed Membrane, then the discrete forcing would reduce to a simple Dirac Comb with no phase change. By setting the incidence angle to zero $\theta_i = 0$, Eqn. 3.14 would simplify to Eqn. 3.12 with the L_1 operator.

3.3.3 Form of the Modified Local Solution

Having determined the linear operator L_2 that efficiently addresses the subtlety of the phase-shifted forcing, the remaining component of the Local Solution $\hat{\eta}_{local}$, termed the "modified Local Solution", can be constructed. The modified Local Solution is assumed to be a piecewise polynomial of the form

$$\hat{\eta}_{local} = \begin{cases} 0 & x \leqslant -L_s \\ \hat{\eta}_l = \sum_{n=0}^{Q} b_n x^n & -L_s < x < 0 \\ \hat{\eta}_r = \sum_{n=0}^{Q} a_n x^n & 0 < x < L_s \\ 0 & x \geqslant -L_s \end{cases} \tag{3.16}$$

Here the modified Local Solution around the discontinuity at the origin is presented. It is beneficial to rescale the modified Local Solution to the smoothing length so

that $\bar{\eta}_{local} = \hat{\eta}_{local}/L_s$, and similarly for all the other variables and constants. This rescaling improves the behavior of the coefficient matrix that will be inverted to determine the coefficients a_n and b_n. The rescaled piecewise polynomial is

$$\bar{\eta}_{local} = \begin{cases} 0 & \bar{x} \leqslant -1 \\ \bar{\eta}_l = \sum_{n=0}^{Q} \bar{b}_n \bar{x}^n & -1 < x < 0 \\ \bar{\eta}_r = \sum_{n=0}^{Q} \bar{a}_n \bar{x}^n & 0 < x < 1 \\ 0 & \bar{x} \geqslant -1 \end{cases} \tag{3.17}$$

3.3.4 Effect of Discontinuous Loading

The Local Solution for ANM is responsible for identifying and treating the effect of the discontinuous loading on the system at the point of application. By integrating the governing equation of $\bar{\eta}_{local}$ (Eqn. 3.15) in x from $-\varepsilon$ to ε

$$\int_{-\varepsilon}^{\varepsilon} L_2[\bar{\eta}_{local}]\, dx = \int_{-\varepsilon}^{\varepsilon} \left(\bar{f}_o \delta(x) - \bar{f}_{structural}\right) dx \tag{3.18}$$

assuming the displacement and distributed forcing to be finite and continuous, and taking the limit as $\delta \rightarrow 0$ yields

$$-\bar{\eta}_l'(\bar{x})|_{\bar{x}=0^-} + \bar{\eta}_r'(\bar{x})|_{\bar{x}=0^+} = -\bar{f}_o \tag{3.19}$$

Thus, it is shown that the discrete force manifests itself as a discontinuity in the slope of the membrane displacement. Using the polynomial form of the Local Solution and evaluating this expression, the first constraint on the polynomial coefficients is determined to be

$$\bar{a}_1 - \bar{b}_1 = -\bar{f}_o \tag{3.20}$$

3.3.5 Development of Local Solution Constraints

In order to determine the coefficients of the modified Local Solution polynomial, a series of constraints are applied at the boundaries of the piecewise regions. The order of the polynomial Q is a result of the number of constraints assigned in order

to generate the Local Solution. The conditions used in this work are presented here. Each constraint is first presented in general notation and is immediately followed by the polynomial representation using Eqn. 3.17.

Continuous displacement at drive point

The displacement of the piecewise modified Local Solution must be continuous at the drive point, so that

$$\hat{\eta}_l\left(\bar{x}\right)\big|_{\bar{x}=0} = \hat{\eta}_r\left(\bar{x}\right)\big|_{\bar{x}=0} \tag{3.21a}$$

$$\bar{b}_0 = \bar{a}_0$$

Zero displacement at smoothing length

Since the Local Solution is zero outside of the smoothing region, the displacement at the smoothing length must be zero so that the membrane is continuous.

$$\hat{\eta}_l\left(\bar{x}\right)\big|_{\bar{x}=-1} = 0, \quad \hat{\eta}_r\left(\bar{x}\right)\big|_{\bar{x}=1} = 0 \tag{3.21b}$$

$$\sum_{n=0}^{Q} \bar{b}_n(-1) = 0, \quad \sum_{n=0}^{Q} \bar{a}_n = 0$$

Smooth displacement at smoothing length

The Local Solution must smoothly approach the zero displacement at the smoothing length to ensure that no discrete force is introduced at the outer edge.

$$\bar{\eta}_l'\left(\bar{x}\right)\big|_{\bar{x}=-1} = 0, \quad \bar{\eta}_r'\left(\bar{x}\right)\big|_{\bar{x}=1} = 0 \tag{3.21c}$$

$$\sum_{n=1}^{Q} n\bar{b}_n(-1)^{n-1} = 0, \quad \sum_{n=1}^{Q} n\bar{a}_n = 0$$

Having defined conditions on the motion of Local Solution at the piecewise boundaries, it is beneficial to introduce conditions on the smoothed forcing in order to

ensure that it is continuous and smooth, thus improving the convergence of the Global Solution.

Continuous Smoothed Force at drive point

Considering the governing equation of the modified Local Solution, a continuous forcing at the drive point requires that

$$-\bar{\eta}''_{local} + 2i\bar{k}_1 \sin\theta_i \bar{\eta}'_{local}\Big|_{0^-}^{0^+} = 0 \tag{3.21d}$$

which is rewritten in terms of the piecewise components as

$$-\bar{\eta}''_l + 2i\bar{k}_1 \sin\theta_i \bar{\eta}'_l\Big|_{0^-} = -\bar{\eta}''_r + 2i\bar{k}_1 \sin\theta_i \bar{\eta}'_r\Big|_{0^+}$$

$$-2\bar{a}_2 + 2i\bar{k}_1 \sin\theta_i \bar{a}_1 = -2\bar{b}_2 + 2i\bar{k}_1 \sin\theta_i \bar{b}_1$$

Continuous Slope of Smoothed Force at drive point

In order to ensure that the distributed force is in fact smooth at the drive point, the slope of the smoothed force is required to be continuous across the point of application. Taking the derivative of the governing equation to determine an expression for the slope of the distributed load and setting the slope on either side of the drive point to be equivalent yields

$$-\bar{\eta}'''_{local} + 2i\bar{k}_1 \sin\theta_i \bar{\eta}''_{local} + \left((\bar{k}_1 \sin\theta_i)^2 - k_M^2\right) \bar{\eta}'_{local}\Big|_{0^-}^{0^+} = 0 \tag{3.21e}$$

$$-6\bar{b}_3 + i4\bar{k}_1 \sin\theta_i \bar{b}_2 + \left((\bar{k}_1 \sin\theta_i)^2 - k_M^2\right) \bar{b}_1 = -6\bar{a}_3 + i4\bar{k}_1 \sin\theta_i \bar{a}_2 + \left((\bar{k}_1 \sin\theta_i)^2 - k_M^2\right) \bar{a}_1$$

Zero Smoothed Force at smoothing length

The distributed force is only applied within the smoothing region, therefore the value of this force must be set to zero at the outer boundaries of the local region to ensure

the distributed load is continuous and no unintentional additional discrete loads are introduced. This is written as

$$-\bar{\eta}''_{local} + 2i\bar{k}_1 \sin\theta_i \bar{\eta}'_{local} + \left((\bar{k}_1 \sin\theta_i)^2 - k_M^2\right) \bar{\eta}_{local}\Big|_{x=\{-1,1\}} = 0 \tag{3.21f}$$

evaluated at both outer boundaries, and using previous conditions on the displacement and slope of the Local Solution at the boundaries, they reduce to

$$-\bar{\eta}''_l\Big|_{x=-1} = 0, \quad -\bar{\eta}''_r\Big|_{x=1} = 0 \tag{3.21g}$$

$$\sum_{n=2}^{Q} n(n-1)(-1)^{n-2}\bar{b}_n = 0, \quad \sum_{n=2}^{Q} n(n-1)\bar{a}_n = 0$$

Continuous Slope of Smoothed Force at smoothing length

Similar to the drive point, the slope of the smoothed force is enforced to be continuous at the outer bounds of the Local Solution, and therefore zero, since it is required to be zero outside of the local region.

$$\bar{\eta}'''_l(\bar{x})\Big|_{\bar{x}=-1} = 0, \quad \bar{\eta}'''_r(\bar{x})\Big|_{\bar{x}=1} = 0, \tag{3.21h}$$

$$\sum_{n=3}^{Q} n(n-1)\bar{b}_n(-1)^{n-3} = 0, \quad \sum_{n=3}^{Q} n(n-1)\bar{a}_n = 0$$

Acoustically Compact Constraint

It is also beneficial to limit the range of influence of the Local Solution through the fluids by requiring this structural motion to be a weak radiator. By requiring that the total area under the Local Solution to be zero, there will be no net monopole strength which is an efficient radiator, and therefore the fluid effects are more localized. Treating each component of the piecewise Local Solution separately, this

condition is written as

$$\int_{-1}^{0} \bar{\eta}_l(\bar{x}) e^{-i\bar{k}_s\bar{x}} d\bar{x} = 0, \quad \int_{0}^{1} \bar{\eta}_r(\bar{x}) e^{-i\bar{k}_s\bar{x}} d\bar{x} = 0 \tag{3.21i}$$

where the complete local displacement has been used (as opposed to the modified local displacement) because that is the motion that affects the actual fluid pressures. Though tedious, these integrals can be evaluated in closed form given that the modified local displacement is a polynomial. For example, the resultant constraints for the simplest case of normal incidence $k_s = 0$ is produced below.

$$\int_{-1}^{0} \bar{\eta}_l d\bar{x} = \sum_{n=0}^{Q} \frac{\bar{b}_n(-1)^{n+1}}{n+1} = 0, \quad \int_{0}^{1} \bar{\eta}_r d\bar{x} = \sum_{n=0}^{Q} \frac{\bar{a}_n}{n+1} = 0 \tag{3.21j}$$

This condition consequently will improve the convergence of the global problem.

3.3.6 Solving for the Local Solution

Having outlined these constraints, solving for the coefficients of the modified Local Solution is a simple matrix inversion problem.

$$\begin{pmatrix}
0 & 1 & 0 & 0 & 0 & 0 & 0 & 0 & -1 & 0 & 0 & 0 & 0 & 0 \\
-1 & 0 & 0 & 0 & 0 & 0 & 0 & 1 & 0 & 0 & 0 & 0 & 0 & 0 \\
1 & 1 & 1 & 1 & 1 & 1 & 1 & 0 & 0 & 0 & 0 & 0 & 0 & 0 \\
0 & 0 & 0 & 0 & 0 & 0 & 0 & 1 & -1 & 1 & -1 & 1 & -1 & 1 \\
0 & 1 & 2 & 3 & 4 & 5 & 6 & 0 & 0 & 0 & 0 & 0 & 0 & 0 \\
0 & 0 & 0 & 0 & 0 & 0 & 0 & 0 & 1 & -2 & 3 & -4 & 5 & -6 \\
0 & 2i\bar{k}_s & -2 & 0 & 0 & 0 & 0 & 0 & -2i\bar{k}_s & 2 & 0 & 0 & 0 & 0 \\
0 & \Delta\bar{k}^2 & 4i\bar{k}_s & -6 & 0 & 0 & 0 & 0 & -\Delta\bar{k}^2 & -4i\bar{k}_s & 6 & 0 & 0 & 0 \\
0 & 0 & 2 & 6 & 12 & 20 & 30 & 0 & 0 & 0 & 0 & 0 & 0 & 0 \\
0 & 0 & 0 & 0 & 0 & 0 & 0 & 0 & 0 & 2 & -6 & 12 & -20 & 30 \\
0 & 0 & 0 & 6 & 24 & 60 & 120 & 0 & 0 & 0 & 0 & 0 & 0 & 0 \\
0 & 0 & 0 & 0 & 0 & 0 & 0 & 0 & 0 & 0 & 6 & -24 & 60 & -120 \\
[& \cdots & \int_0^1 \bar{x}^n e^{-i\bar{k}_s\bar{x}} d\bar{x} & \cdots &] & 0 & 0 & 0 & 0 & 0 & 0 & 0 & 0 & \\
0 & 0 & 0 & 0 & 0 & 0 & 0 & [& \cdots & \int_0^1 \bar{x}^n e^{-i\bar{k}_s\bar{x}} d\bar{x} & \cdots & & &]
\end{pmatrix}
\begin{pmatrix} \bar{a}_0 \\ \bar{a}_1 \\ \bar{a}_2 \\ \bar{a}_3 \\ \bar{a}_4 \\ \bar{a}_5 \\ \bar{a}_6 \\ \bar{b}_0 \\ \bar{b}_1 \\ \bar{b}_2 \\ \bar{b}_3 \\ \bar{b}_4 \\ \bar{b}_5 \\ \bar{b}_6 \end{pmatrix} =
\begin{pmatrix} -\bar{f}_o \\ 0 \\ 0 \\ 0 \\ 0 \\ 0 \\ 0 \\ 0 \\ 0 \\ 0 \\ 0 \\ 0 \\ 0 \\ 0 \end{pmatrix}$$

where $\Delta\bar{k}^2 \equiv \left(\bar{k}_1^2 \sin^2\theta_i - k_M^2\right)$ has been temporarily introduced for presentation of the matrix equation. It is important to note that the formulation of the Local Solution is not unique but rather there is flexibility in the constraints that can be applied

to improve the convergence of the smoothed forcing. However, improving the convergence of the smoothed forcing by requiring higher derivatives to be smooth increases the complexity of the Local Solution formulation with diminishing returns.

Once the coefficients of the modified Local Solution $\bar{a}_n$ and $\bar{b}_n$ are determined, they can be rescaled to the distance separating the discrete forces (the length scale used throughout the non-dimensionalization scheme). Finally, the fully constructed Local Solution with the phase shift information can be assembled as

$$\eta_{local} = \begin{cases} 0 & x \leqslant -L_s \\ \eta_l = \left(\sum_{n=0}^{Q} b_n x^n\right) e^{-ik_1 \sin\theta_i x} & -L_s < x < 0 \\ \eta_r = \left(\sum_{n=0}^{Q} a_n x^n\right) e^{-ik_1 \sin\theta_i x} & 0 < x < L_s \\ 0 & x \geqslant -L_s \end{cases} \tag{3.22}$$

Figures 3.3 and 3.4 portray the real displacement and phase, respectively, of a Local Solution with a discrete force at $x = 0$, with forcing frequency $k_1 = 15$, incidence angle $\theta_i = \dfrac{\pi}{4}$, in-vacuo wavenumber $k_M = 30$, and smoothing length of $L_s = 0.1$. This represents a Local Solution that is constrained to within 10% of the bay length. A small smoothing length is beneficial for the acoustical compactness. The choice of smoothing length is a compromise between making the Local Solution a weak radiator and convergence considerations.

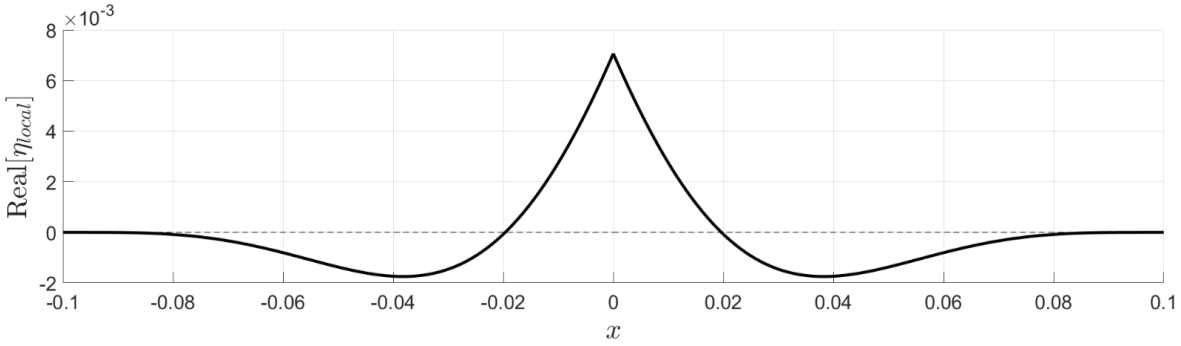

FIGURE 3.3: Real part of Local Solution displacement within the smoothing region

From this figure, it is straightforward to see how the imposed constraints manifest

themselves into the shape of Local Solution. The real part of the displacement is shown to clearly represent that the area under the curve is zero.

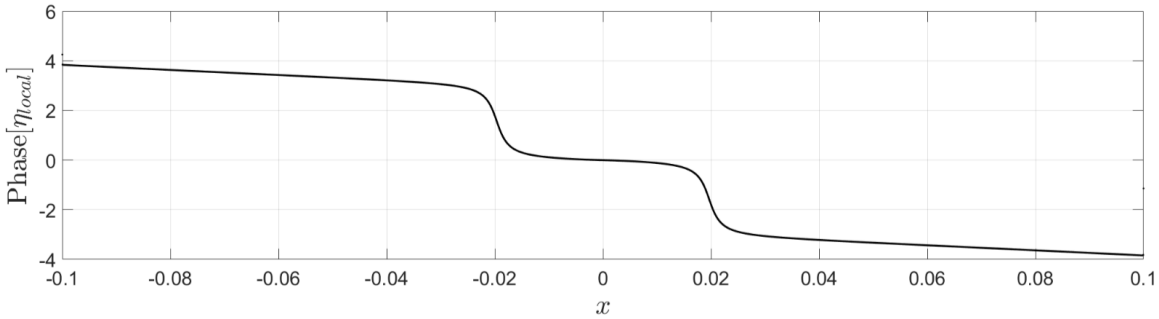

FIGURE 3.4: Phase of Local Solution displacement within the smoothing region

In the phase plot above, the most important characteristic is that the phase is continuous at the drive point, and therefore the Local Solution is confirmed to be both continuous in amplitude and phase. The non-zero values of the phase at the smoothing lengths are not an issue because the amplitude at that location is set to zero, and therefore there is no violation in continuity.

3.4 Global Problem

Having determined the displacement of the membrane in the Local Solution without approximation, the smoothed forcing and coupled fluid pressures from the local motion can be described in order to define and modally solve the Global Problem. As restated below in the governing equation of the global problem, the fluid pressures coupled to the Global Solution are also needed.

$$L_1 \left[\eta_{global}\right] = f_{structural}\left(x\right) - p_s^{local} - p_s^{global} \tag{3.23}$$

3.4.1 Modal Description of the Smoothed Forcing

The smoothed forcing is the distributed load applied to the Global Problem in order to determine the overall low resolution motion of the membrane. The modified

smoothed forcing is evaluated using the governing equation of the membrane Eqn. 3.15, which is reproduced below

$$\hat{f}_{structural} = -L_2[\hat{\eta}_{local}] + f_o\delta(x-n)$$

The discrete force is easily implemented in practice because the modified local motion of the membrane was designed to exactly balance it. The polynomial description of the modified Local Solution is substituted into the governing equation, and the resultant loading for the Local Solution shown in Figure 3.3 is plotted below.

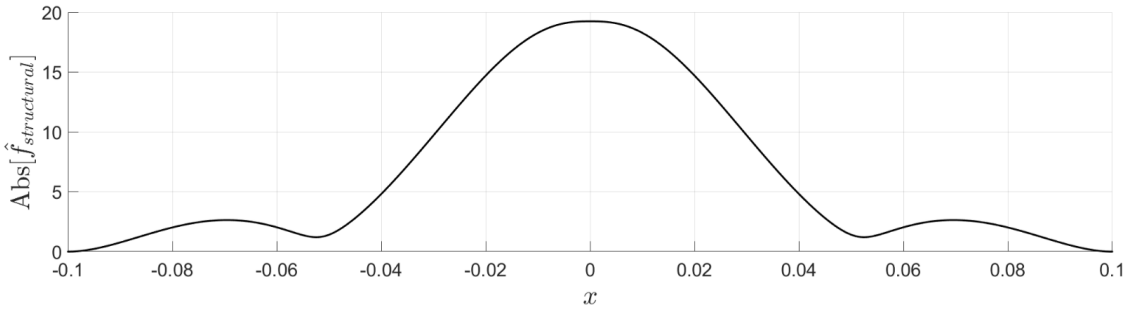

FIGURE 3.5: Absolute value of resultant smooth forcing within the smoothing region

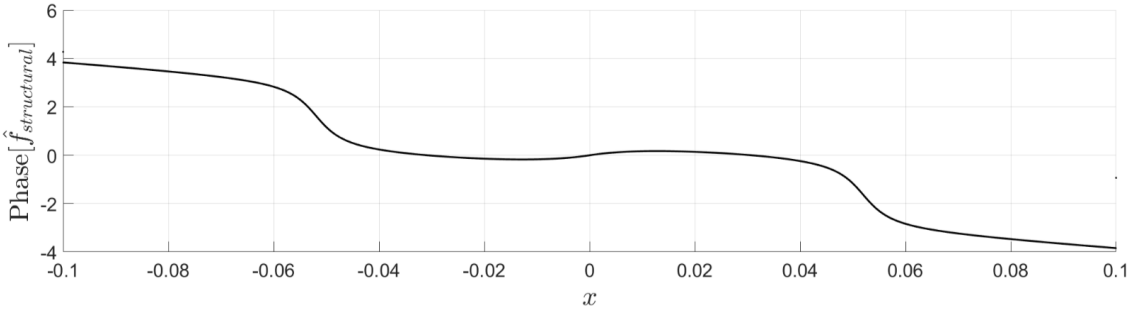

FIGURE 3.6: Phase of resultant smooth forcing within the smoothing region

Since the resultant forcing was designed to be smooth, its modal decomposition quickly converges. The complex Fourier Decomposition, outlined below, takes advantage of the property that the Local Solution and resultant smoothed force is zero

outside of the smoothing region, and is replicated at every drive point.

$$\hat{f}_{structural} = \sum_{m=-\infty}^{\infty} \hat{f}_{structural,m} \cdot e^{i2\pi mx} \tag{3.24a}$$

$$\hat{f}_{structural,m} = \int_{-L_s}^{0} \hat{f}_{structural}(x) \cdot e^{-i2\pi mx} dx + \int_{0}^{L_s} \hat{f}_{structural}(x) \cdot e^{-i2\pi mx} dx \tag{3.24b}$$

The smooth forcing can be interpreted as a distributed load that replaces the discrete force of the original problem statement, and the Local Solution is the difference between these two system responses. The magnitude of the Fourier coefficients of both the smoothed forcing and the discrete forcing are plotted below.

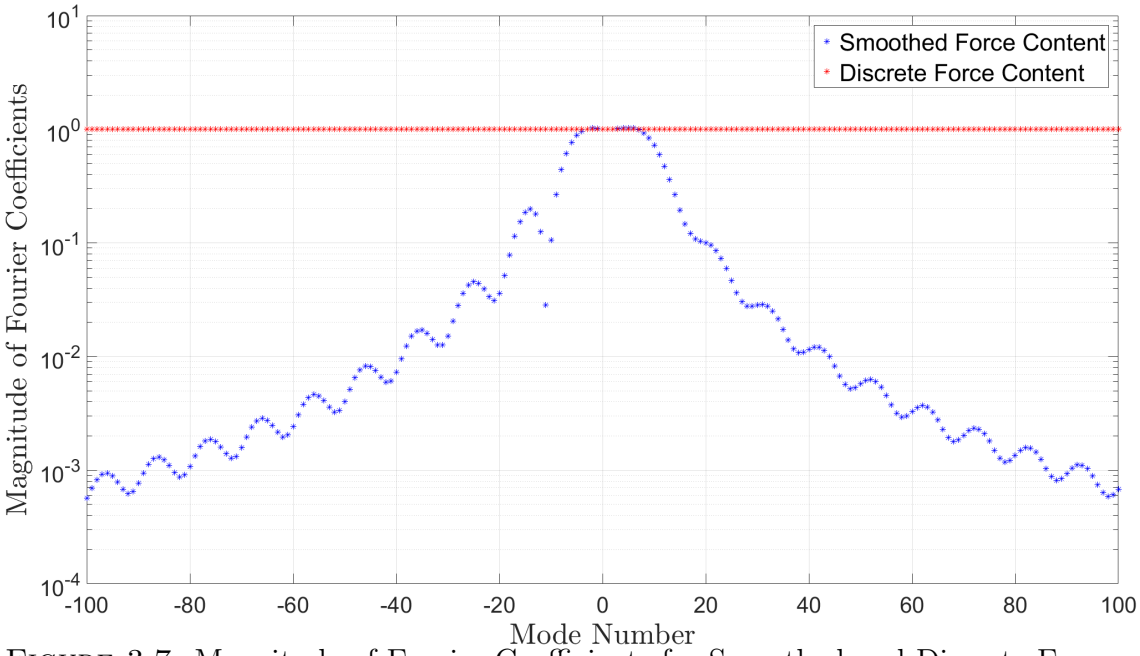

FIGURE 3.7: Magnitude of Fourier Coefficients for Smoothed and Discrete Forces

Unlike the discrete load, the smoothed force is lacking in higher modal content. This property confirms that the Global Solution - the response of the membrane to this loading - will predominantly describe the overall motion of the membrane described by the lower resolution modal content.

Similarly, the contributions from the fluid loading are also smooth and are described using a modal decomposition with the same eigenfunctions as above.

3.4.2 Modal Description of Fluid Pressures from Local Solution

Having prescribed the modified Local Solution, the surface pressures are also known by satisfying the boundary condition of continuous vertical velocity and use of the momentum equation as shown in Eqn. 3.4. In order to determine the modal description of the fluid surface pressures, the modified local displacement must be modally decomposed. Again using a complex Fourier decomposition, the modified Local Solution is rewritten as

$$\hat{\eta}_{local} = \sum_{m=-\infty}^{\infty} \hat{\eta}_{local,m} \cdot e^{i2\pi mx} \tag{3.25a}$$

$$\hat{\eta}_{local,m} = \int_{-L_s}^{0} \hat{\eta}_l(x) \cdot e^{-i2\pi mx} dx + \int_{0}^{L_s} \hat{\eta}_r(x) \cdot e^{-i2\pi mx} dx \tag{3.25b}$$

As before, the Local Solution with the phase information is constructed from the modified Local Solution using the relationship in Eqn. 3.13a, such that

$$\eta_{local} = \left(\sum_{m=-\infty}^{\infty} \hat{\eta}_{local,m} \cdot e^{i2\pi mx} \right) e^{-ik_1 \sin\theta_i x} = \sum_{m=-\infty}^{\infty} \hat{\eta}_{local,m} \cdot e^{-ik_{x,m} x} \tag{3.26a}$$

where the wavenumber component in the x-direction is modally defined as

$$k_{x,m} = k_1 \sin\theta_i - 2\pi m \tag{3.26b}$$

It is important to note that when interested in the motion of the structure, the Local Solution is not modally decomposed; rather the exact polynomial description of the Local Solution is employed. The modal decomposition of the Local Solution is only used in determining the smooth distributed load and far field pressures (considered in Section 3.7.2). The modal decomposition of the modified Local Solution can then be used to determine the fluid surface pressures acting on the membrane.

$$\hat{p}_{s,m}^{local} = -\left(\frac{k_1}{M_1}\right)^2 \left(\frac{\varepsilon_1}{\sqrt{k_{x,m}^2 - k_1^2}} + \frac{\varepsilon_2}{\sqrt{k_{x,m}^2 - k_2^2}} \right) \hat{\eta}_{local,m} \tag{3.27}$$

$$p_s^{local} = \sum_{m=-\infty}^{\infty} \hat{p}_{s,m}^{local} \cdot e^{-ik_{x,m}x} \tag{3.28}$$

In Figure 3.8 below, the magnitude of these Fourier coefficients describing the fluid pressures at the surface due to the motion of the Local Solution from Figure 3.3 are plotted along with the modal amplitudes of the smooth forcing. For this sample case, the fluids on either half space of the structure are assumed to be identical with properties $\varepsilon_1 = \varepsilon_2 = 10$, and $M_1 = M_2 = 0.5$. These characteristic parameter values will be used throughout the remainder of this work, unless specifically noted otherwise.

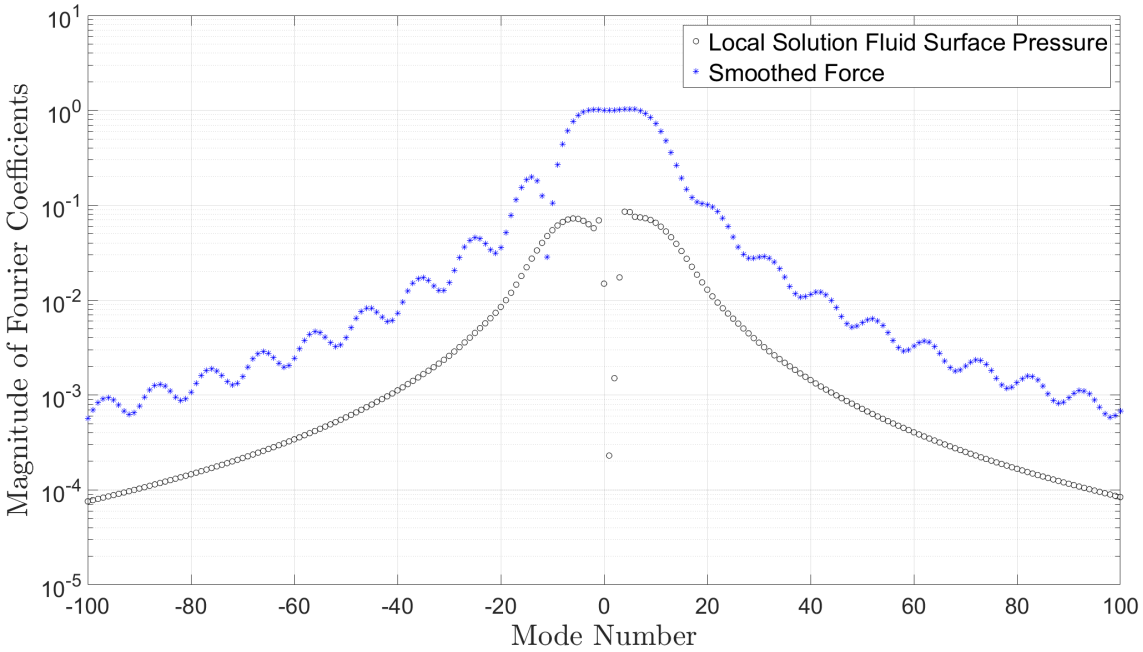

FIGURE 3.8: Magnitude of Fourier Coefficients for Smoothed and fluid surface pressure from Local Solution

The decreasing magnitude of the Fourier coefficients confirms that there is little higher mode content in the fluid pressures from the Local Solution motion, and these pressures are therefore smooth and quickly converge. This validates the modal treatment, and therefore its allocation to the Global Problem formulation, of these

fluid pressures from the quickly varying Local Solution. The magnitude of the modal coefficients for the fluid pressures around the zeroth mode are markedly small as a result of the zero area under the curve constraint on the Local Solution.

3.4.3 Solving for Global Solution

As a result of the functional form of the forcing terms, the Global Solution is assumed to have the form of

$$\eta_{global} = \sum_{m=-\infty}^{\infty} \eta_{global,m} e^{-ik_{x,m}x} \tag{3.29}$$

A similar expression to Eqn. 3.28 can be written for the fluid pressures coupled to the global motion.

$$p_{s,m}^{global} = -\left(\frac{k_1}{M_1}\right)^2 \left(\frac{\varepsilon_1}{\sqrt{k_{x,m}^2 - k_1^2}} + \frac{\varepsilon_2}{\sqrt{k_{x,m}^2 - k_2^2}}\right) \eta_{global,m} \tag{3.30}$$

Substituting the modal descriptions of the expressions in Eqn. 3.23 and solving the governing equation yields the coefficients of the Global Solution as

$$\eta_{global,m} = \frac{\hat{f}_{structural,m} + \left(\frac{k_1}{M_1}\right)^2 \left(\frac{\varepsilon_1}{\sqrt{k_{x,m}^2 - k_1^2}} + \frac{\varepsilon_2}{\sqrt{k_{x,m}^2 - k_2^2}}\right) \hat{\eta}_{local,m}}{\left[k_{x,m}^2 - k_M^2\right] - \left(\frac{k_1}{M_1}\right)^2 \left(\frac{\varepsilon_1}{\sqrt{k_{x,m}^2 - k_1^2}} + \frac{\varepsilon_2}{\sqrt{k_{x,m}^2 - k_2^2}}\right)} \tag{3.31}$$

Having determined the coefficients of the Global Solution decomposition, the motion of the Driven Membrane can be assembled.

3.5 Driven Membrane: Assembly of ANM Solution

The total displacement of the Driven Membrane η_{driven} is the sum of the smooth Global Solution and the quickly varying Local Solution near the drive points.

$$\eta_d = \eta_{global} + \eta_{local} \tag{3.32}$$

Figure 3.9 below shows the magnitude of the membrane displacement in the global and Local Solution, as well as the composite displacement around the drive point at the origin.

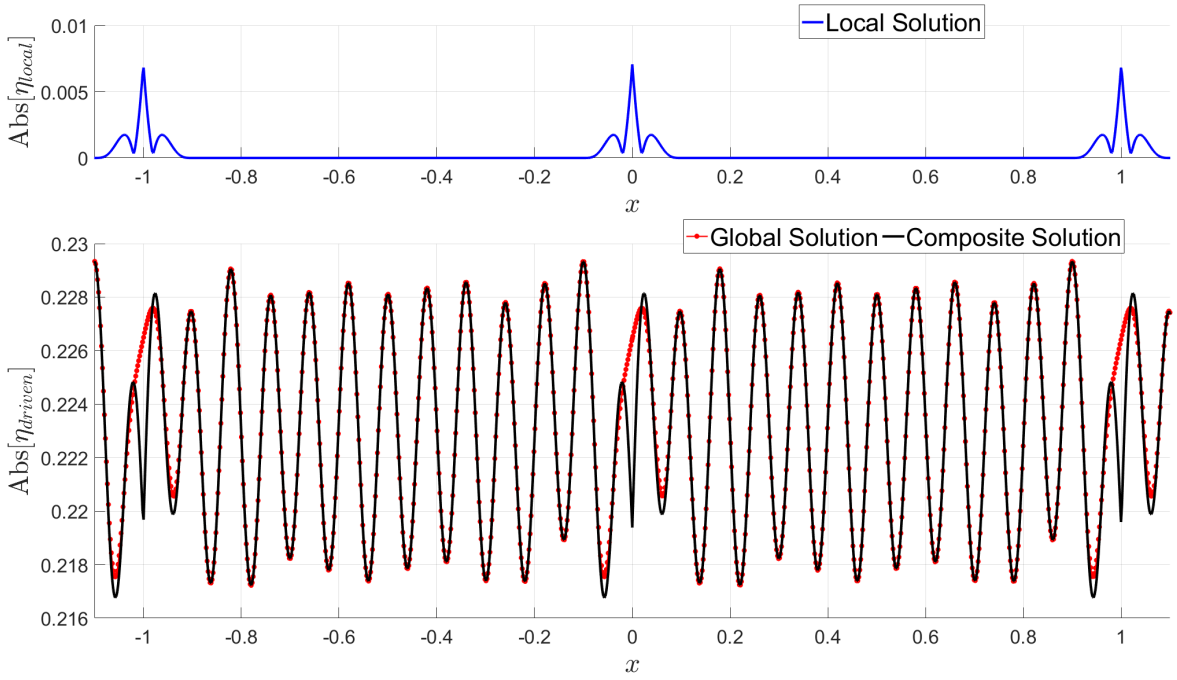

FIGURE 3.9: Magnitudes of structure displacement from the (Top) Local Solution and (Bottom) global and composite solutions of the driven membrane.

This figure illustrates that the Global Solution accurately describes the overall motion of the membrane away from the drive points: the lower resolution content. The Local Solution analytically treats the high resolution content near the drive points, and is zero outside of the smoothing region. Adding the global and Local Solutions wholly describes the total motion of the Driven Membrane.

3.6 Comparison of ANM to Classical Modal Approach

The composite ANM solution is compared to the Classical Modal Solution in order to confirm the validity of the method, as well as further explore the characteristics and benefits of the ANM solution.

3.6.1 Classical Modal Decomposition

The Classical Solution consists of a completely modal treatment of the equation of motion of the Driven Membrane from Eqn.3.6. This governing equation is rewritten using the Modified Linear Operator L_2 presented in Section 3.3.2 to treat the discrete force phase shift. Using the same eigenfunctions as in the ANM treatment, the Classical Solution for the Driven Membrane displacement η_c is modeled as

$$\eta_c = \sum_{m=-\infty}^{\infty} \hat{\eta}_{c,m} e^{-ik_{x,m}x} \tag{3.33a}$$

$$\hat{\eta}_{c,m} = \frac{f_o}{(2\pi m)^2 - 4\pi k_1 \sin\theta_i m + [(k_1 \sin\theta_i)^2 - k_M^2] - \left(\frac{k_1}{M_1}\right)^2 \left(\frac{\varepsilon_1}{\sqrt{k_{x,m}^2 - k_1^2}} + \frac{\varepsilon_2}{\sqrt{k_{x,m}^2 - k_2^2}}\right)} \tag{3.33b}$$

3.6.2 Convergence Comparison of Methods

The Classical and ANM solutions are compared by plotting the magnitude of the Fourier coefficients for both solutions in Figure 3.10. For this analysis, the modal decomposition of the Local Solution is used and added to the Global Solution Fourier coefficients to determine the modal description of the Composite ANM solution.

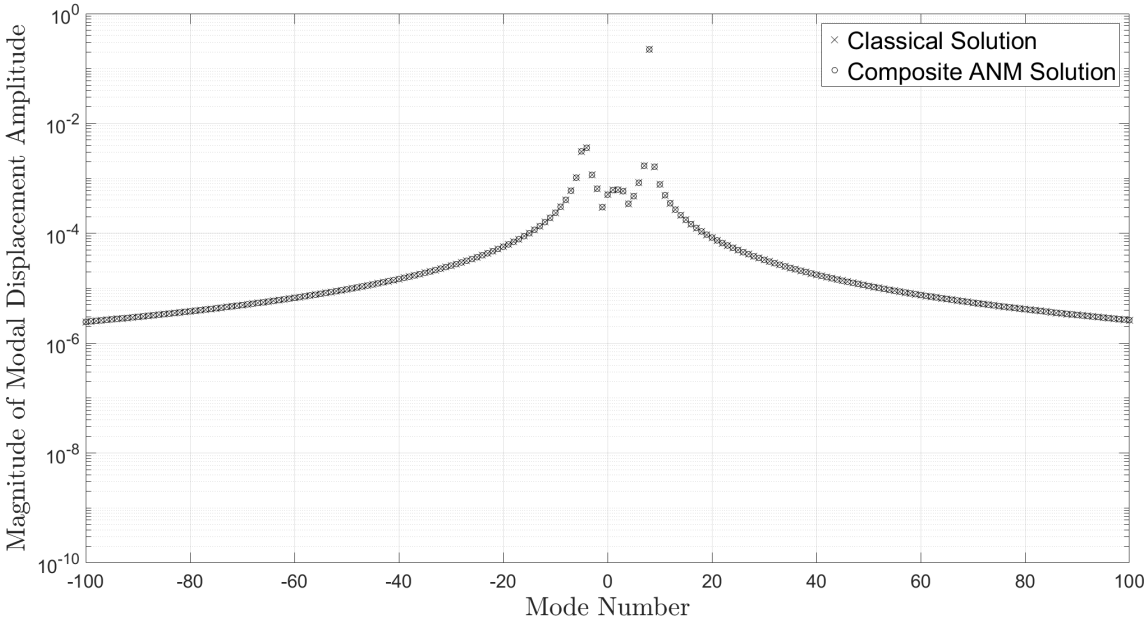

FIGURE 3.10: Magnitude of Fourier Coefficients of structural displacement; Classical and Composite ANM Solutions

The plot above shows the magnitude of the harmonics for both solutions to be equivalent on a mode-by-mode comparison. This confirms that in the absence of truncation errors, the composite ANM solution is identical to the Classical Solution.

Plotting the harmonic magnitudes of the Global and Local Solutions effectively demonstrates the role of the ANM components. In Figure 3.11 below, the modal distributions of the two ANM components are plotted alongside that of the Classical Solution. It is clear that the Global Solution dominates the low mode number content where it matches the Classical Solution. It then falls off orders of magnitude faster than the Classical Solution, thus justifying the previous statements that the Global Solution quickly converges. The Local Solution is designed to capture the high resolution content near the drive points, and this is evident by its rising to match the Classical Solution at the larger mode numbers.

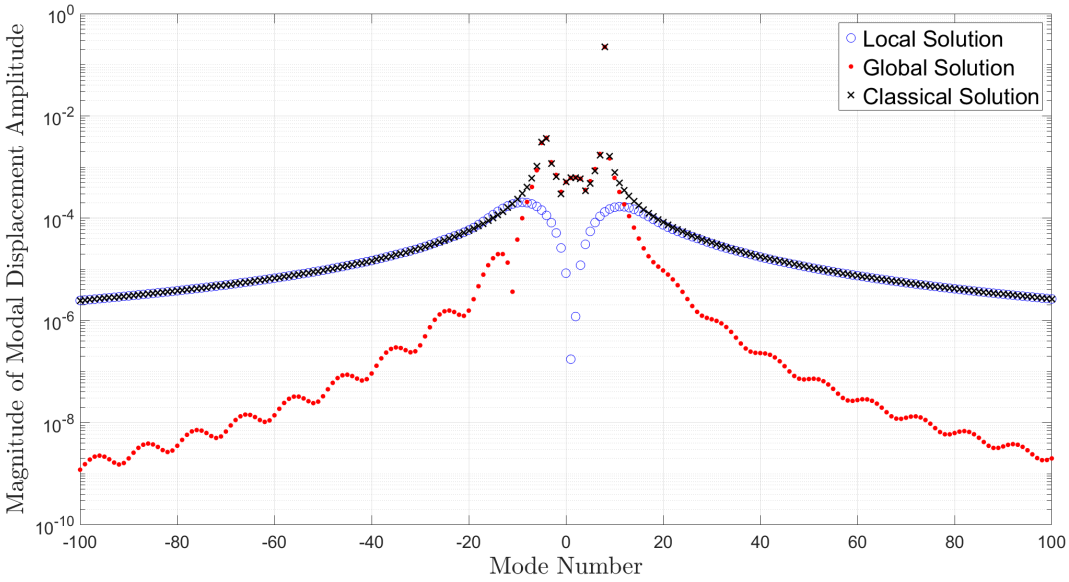

FIGURE 3.11: Magnitude of Fourier Coefficients of structural displacement; Classical Solution and ANM Components

One of the significant advantages of ANM that is perhaps obscured by this figure is that the Local Solution is an exact analytical expression and was only decomposed here for illustrative purposes. In practice the analytical expression is used. The known polynomial contains all of the harmonic information without any truncation error, which improves the convergence and decreases the computational effort as compared to the Classical Solution. Comparing the convergence of the two methods is achieved by evaluating the percent error relative to a modal solution that was converged to a much greater accuracy than the truncated series evaluated here. The first metric considered compares the absolute value of the spatially averaged membrane displacement error. The percent error is plotted against the number of modes used in the series solution. Figure 3.12 shows that for a given number of evaluated modes, the ANM solution results in a smaller percent error than the Classical Solution. Additionally, as the number of modes increases, the percent error decreases more rapidly for the ANM solution.

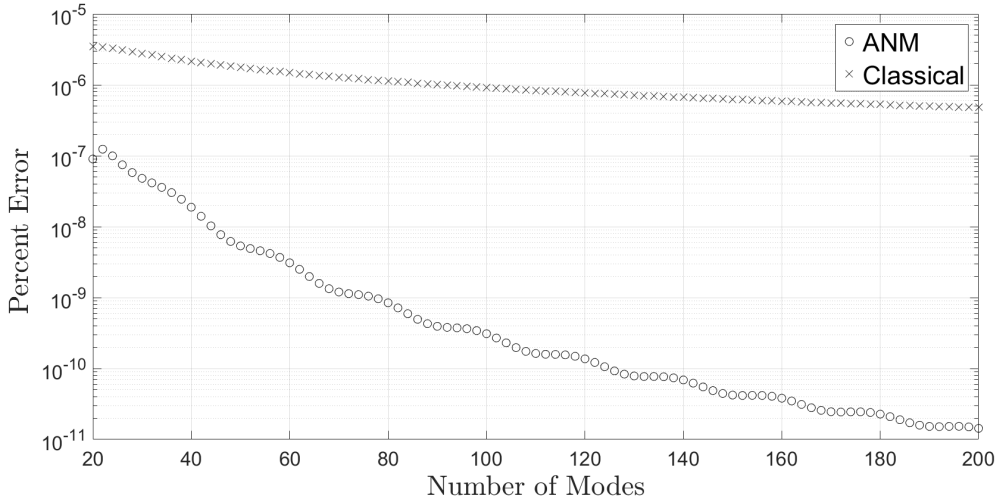

FIGURE 3.12: Convergence of structural displacement spatial average for Driven Membrane; Classical and ANM Solutions

Examining the Classical Solution, it can be argued that although the spatial average is slowly converging, the percent error for the spatial average is not significant for this particular set of parameters, even with the use of few modes. This suggests that for this configuration, and most all others, the Classical modal treatment does describe the overall motion of the structure accurately. However, as previously stated, it does not efficiently treat the slowly convergent region near the drive point. This characteristic is investigated by considering the absolute value of the membrane displacement at the drive point. In Figure 3.13, the percent error of this displacement magnitude is plotted against the number of modes used in the series solution and is compared to a series solution that has converged well beyond the errors presented here. It is clear that for a given number of evaluated modes, the ANM solution results in a smaller percent error than the Classical Solution for the magnitude of the drive point displacement. Additionally, as the number of modes increases, the percent error decreases more rapidly for the ANM solution. The ANM method is specifically designed to efficiently treat the high resolution content at and near the drive point that slowly converges when using the Classical modal treatment.

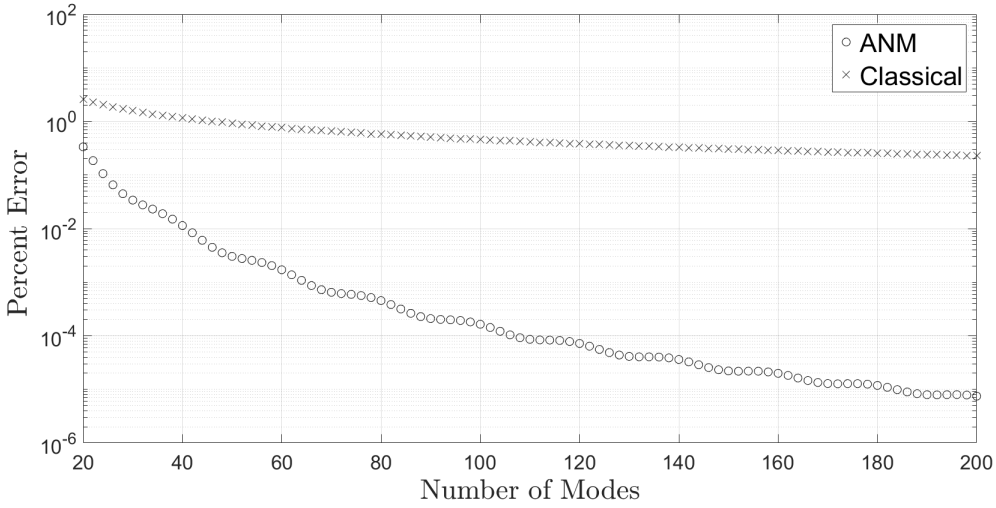

FIGURE 3.13: Convergence of structural displacement at drive point for Driven Membrane; Classical and ANM Solutions

Efficiently describing the displacement at the drive point is crucial for the accurate prediction of the structural motion of the periodically fixed membrane. As outlined in Section 1.1.1, the Driven Membrane motion is inversely proportional to its displacement at the drive point in order to scale to the Unconstrained Membrane motion and bring the Periodically Fixed Membrane to rest at the constraint points. This scaling is detailed in Eqn. 1.1, which is rewritten here as

$$\eta_{total} = \eta_{free} - \lambda \cdot \eta_d \tag{3.34}$$

and the scaling factor λ is defined as

$$\lambda = \left(\frac{\eta_{free}}{\eta_d} \right) \Bigg|_{x=0} \tag{3.35}$$

The accuracy of the scaled Driven Membrane motion, and therefore the Periodically Fixed Membrane motion, is controlled by the accuracy of the drive point displacement. This is critical because as demonstrated, the drive point displacement converges slowly compared to the overall motion. Any numerical error in determining

the drive point motion will negatively influence the entire Driven Membrane motion. ANM is specifically designed to efficiently treat these slowly converging regions by describing them analytically, thereby reducing the error due to series truncation. This makes the ANM method particularly powerful when applied to problems with structural discontinuities whose overall response scales with the high resolution motion at and near the discontinuity.

3.7 Resultant Acoustic Fields

The fluid pressures on the surface of the structure were used to determine the coupled motion of the Driven Membrane. Having determined both the Local and Global Solutions, the pressure fields in both fluid spaces coupled to the motion of the Driven Membrane can be specified. Using the pressure field expressions determined in Eqn. 3.4, the pressure fields due to the Driven Membrane in the top fluid p_{D1} and the bottom fluid p_{D2} can be modally described as

$$p_{D1} = \sum_{m=-\infty}^{\infty} -\left(\frac{k_1}{M_1}\right)^2 \frac{\varepsilon_1}{\sqrt{k_{x,m}^2 - k_1^2}} \left[\eta_{g,m} + \hat{\eta}_{local,m}\right] e^{i\left(-k_{x,m}x + i\sqrt{k_{x,m}^2 - k_1^2}y\right)} \tag{3.36a}$$

$$p_{D2} = \sum_{m=-\infty}^{\infty} \left(\frac{k_1}{M_1}\right)^2 \frac{\varepsilon_2}{\sqrt{k_{x,m}^2 - k_2^2}} \left[\eta_{g,m} + \hat{\eta}_{local,m}\right] e^{i\left(-k_{x,m}x - i\sqrt{k_{x,m}^2 - k_2^2}y\right)} \tag{3.36b}$$

where the wavenumber component in the x-direction is $k_{x,m} = k_1 \sin\theta_i - 2\pi m$. For the Periodically Fixed Membrane, this thesis focuses on the acoustic field far from the membrane relative to the acoustic wavelength. The far-field pressures from the Driven Problem are investigated in the following sections.

3.7.1 The Discrete Spectrum

The first characteristic noted of both acoustic fields from the Driven Problem is that they are described by a discrete spectrum, which allows them to be described using

an infinite series as shown. This discrete spectrum corresponds to pressure waves in both fluids at an infinite number of angles. The angles, measured from the normal to the membrane, can be determined from the wavenumber components to be

$$\cos\theta_{1,m} = \frac{k_{y1,m}}{k_1} = \frac{-i\sqrt{\left(k_1 \sin\theta_i - 2\pi m\right)^2 - k_1^2}}{k_1} \tag{3.37a}$$

$$\cos\theta_{1,m} = \frac{k_{y1,m}}{k_1} = \frac{-i\sqrt{\left(k_1 \sin\theta_i - 2\pi m\right)^2 - k_1^2}}{k_1} \tag{3.37b}$$

where $\theta_{1,m}$ is the angle of the pressure content from mode m into the top fluid and similarly $\theta_{2,m}$ is the angle into the bottom fluid. It is immediately evident that these angles can be either imaginary or real. This distinction corresponds to evanescent and radiating waves, respectively. In order to describe the far-field pressures, the radiating waves are determined.

3.7.2 Cut-off Phenomenon

Examining the wavenumber component in the y-direction, it is clear that the acoustic fields of the Driven Membrane exhibit the behavior of acoustic cut-off [7, p.492] That is, for a given frequency k_1 and incidence angle θ_i, there are only a finite number of propagating modes. The remaining infinite number of modes generate evanescent waves. The mode numbers that generate radiating waves into the top fluid are within the interval of

$$\frac{k1 \sin\theta_i - k1}{2\pi} < m_{Rad1} < \frac{k1 \sin\theta_i + k1}{2\pi} \tag{3.38a}$$

and the mode numbers that generate propagating waves into the bottom fluid are within the interval of

$$\frac{k1 \sin\theta_i - k_2}{2\pi} < m_{Rad2} < \frac{k1 \sin\theta_i + k_2}{2\pi} \tag{3.38b}$$

With this system having the property of acoustic cut-off, acoustic coincidence can occur and causes mathematical difficulties.

3.7.3 ANM Treatment of Acoustic Coincidence

Acoustic coincidence occurs when the wavenumber on the structure $k_{x,m}$ exactly matches the acoustic wavenumber (either k_1 or k_2), and therefore the wavenumber component in the propagating direction $k_{y,m}$ is zero. The conditions for the modes m_* for which coincidence occurs are defined as

$$k_{y1,m} = \sqrt{k_1^2 - (k_1 \sin\theta_i - 2\pi m_*)^2} = 0 \tag{3.39a}$$

$$k_{y2,m} = \sqrt{k_2^2 - (k_1 \sin\theta_i - 2\pi m_*)^2} = 0 \tag{3.39b}$$

for the top and bottom fluids respectively. For a given frequency and incidence angle, there may not exist a mode m_* where coincidence occurs. However, when it does occur, it results in an infinite pressure contribution at that mode because of the divide-by-zero in Eqns. 3.41, which is not physically consistent for finite structural motion.

Acoustic Coincidence Constraint

The ANM framework, particularly the construction of the Local Solution, allows for a mechanism to deal with this mathematical difficulty. As previously stated, the choice of Local Solution and its constraints are not unique. Therefore, the Local Solution can be designed to be deprived of modal content at the coincidence mode. If the Local Solution has no displacement amplitude at this mode then the smoothed forcing will also lack content at this mode. With no structure motion, there will likewise be no coupled pressure perturbations at this mode. Finally, with no forcing acting on the Global Problem, the Global Solution will also lack modal content at the coincidence mode: the global displacement and its consequent coupled pressures

will be zero. Therefore, by requiring that the Local Solution be orthogonal to the coincidence mode, the coupled pressures at this mode are known to be zero. This constraint is written as

$$\int_{-L_s}^{L_s} \hat{n}_{local}(x) e^{-i2\pi m_*} dx = 0 \tag{3.40}$$

This condition is separated into the piecewise components of the Local Solution and introduced into the coefficient matrix from Section 3.3.6. Incorporating this coincidence constraint increases the order of the Local Solution polynomial, but addresses the mathematical difficulty that results in infinite pressures.

3.7.4 Radiating Pressure Waves from Driven Membrane

Having dealt with the issue of acoustic coincidence, the radiating waves for each fluid medium can be defined as

$$p_{D1,Rad} = \sum_{m_{Rad1}} i \left(\frac{k_1}{M_1}\right)^2 \frac{\varepsilon_1}{\sqrt{k_1^2 - k_{x,m}^2}} \left[\eta_{g,m} + \hat{\eta}_{local,m}\right] e^{i\left(-k_{x,m}x - \sqrt{k_1^2 - k_{x,m}^2}y\right)} \tag{3.41a}$$

$$p_{D2,Rad} = \sum_{m_{Rad2}} -i \left(\frac{k_1}{M_1}\right)^2 \frac{\varepsilon_2}{\sqrt{k_2^2 - k_{x,m}^2}} \left[\eta_{g,m} + \hat{\eta}_{local,m}\right] e^{i\left(-k_{x,m}x + \sqrt{k_2^2 - k_{x,m}^2}y\right)} \tag{3.41b}$$

where m_{Rad1} and m_{Rad2} are defined as the interval of radiating modes in Eqn. 3.38, and the wavenumber expressions have been recast to represent that the waves are radiating. These far-field acoustic pressures will be considered in the framework of the Periodically Fixed Membrane and the overall intensity distribution will be plotted.

4

Periodically Fixed Membrane and Acoustic Fields

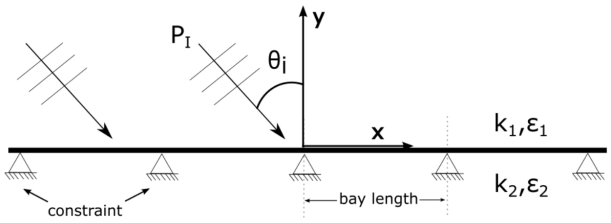

FIGURE 4.1: Periodically Fixed Membrane with an Oblique Acoustic Wave

The previous two chapters delineated the approach for treating the two subproblems referred to as the Unconstrained Membrane and the Driven Membrane. The response of these two systems are scaled and superimposed to construct the response of the Periodically Fixed infinite membrane, including the coupled acoustic fields.

4.1 Scaling and Superposition: Membrane Motion

The structural motion of the Driven Membrane is scaled to the response of the Unconstrained Membrane to construct the membrane motion for the Periodically Fixed Membrane and bring the net displacement to rest at the constraint locations. In Sec-

tion 3.6.2 it was demonstrated that the drive point displacement converges slowly for the Driven Membrane when treated with classical modal methods. Consequently, any error in the drive point displacement corrupts the accuracy of the net motion of the Periodically Fixed Membrane. Therefore, the model developed using the ANM method is used since it is designed to efficiently treat this high resolution region and therefore reduce the error in determining the Periodically Fixed Membrane motion. Continuing with the parameters values used in our previous examples and applying the scaling stated in Eqn. 3.34, the real part of the Periodically Fixed Membrane motion over two bays is plotted below.

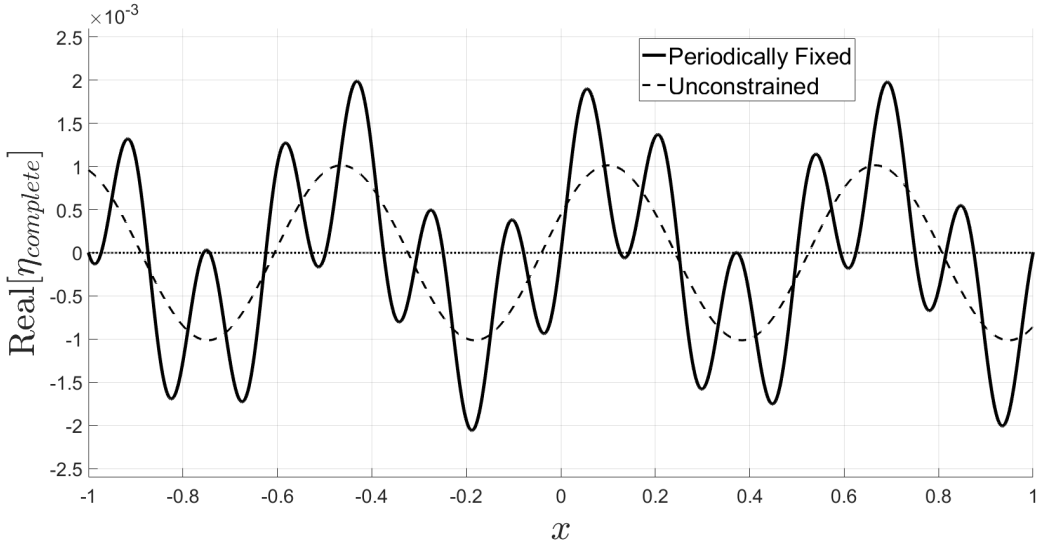

FIGURE 4.2: Real part of Periodically Fixed Membrane motion. Unconstrained Membrane shown for comparison

The motion of the corresponding Unconstrained Membrane is also shown in Figure 4.2 for comparison. This juxtaposition of the two configurations allows for an illustrative representation of the effect of the structural discontinuities included in the Periodically Fixed Membrane. It is immediately confirmed that the displacement at the constraint locations (at integer values of x) is brought to rest for the Periodically Fixed Membrane. Additionally, it is clear that while the Unconstrained

Membrane has only one structural wave (equivalent to the component of the incident wave tangent to the structure), the Complete problem has a spectrum of structural wave numbers, which is an effect of the discontinuities. In Chapter 3 it was shown that this is an infinite discrete spectrum of structural wave numbers.

4.2 Scaling and Superposition: Acoustic Fields

Just as the displacement of the Driven Membrane has to be scaled to the Unconstrained motion, the coupled fluids pressures from the Driven Membrane must also be proportionally scaled by λ to construct the Periodically Fixed Membrane fluid pressures. The resultant far-field pressures due to the motion of the periodically fixed infinite membrane are therefore defined as

$$p_1 = p_R - \lambda \cdot p_{D1,Rad} \tag{4.1a}$$

$$p_2 = p_T - \lambda \cdot p_{D2,Rad} \tag{4.1b}$$

It is convenient to rewrite these far-field pressure contributions using the magnitude and phase of the complex pressure amplitudes as

$$p_1(x,y,t) = |P_R| e^{i\phi_R} e^{i(k_1 t - k_{x1} x - k_{y1} y)} - \sum_{m_{Rad1}} |P_{D1,m}| e^{i\phi_{D1,m}} e^{i(k_1 t - k_{x,m} x - k_{y1,m} y)} \tag{4.2a}$$

$$p_2(x,y,t) = |P_T| e^{i\phi_T} e^{i(k_1 t - k_{x2} x + k_{y2} y)} - \sum_{m_{Rad2}} |P_{D2,m}| e^{i\phi_{D2,m}} e^{i(k_1 t - k_{x,m} x + k_{y2,m} y)} \tag{4.2b}$$

where the amplitudes $P_{D1,m}$ and $P_{D2,m}$ are the scaled Driven Membrane pressure contributions, and the variable ϕ represents the phase of the corresponding complex pressure amplitude.

These expressions for the far-field only consider only the radiating modes; if investigating the acoustic fields close to the structure (relative to the wavelength), then the infinite series would need to be used for the Driven Membrane pressures, but

the scaling and superposition would remain the same. From these expressions, it is clear that accurately describing the scattered acoustic fields is sensitive to the error associated with describing the motion at the drive-point from the Driven Membrane. Every modal amplitude of the far-field pressures from the Driven Membrane is inversely proportional to the displacement of the drive-point, which is the most slowly convergent region of the problem. For the radiated pressures from a driven structure, there is a finite number of modes that result in propagating waves and so these far-field pressure fields are known in closed form without truncation error [1]. However, for a scattering problem influenced by a structural discontinuity, the finite number of radiating modes are scaled by the motion of the drive point which is described by a slowly converging infinite series. Therefore, every radiating mode will be corrupted by the truncation error of the drive-point displacement series. As previously shown, the ANM method is designed to efficiently treat precisely this high resolution region, and therefore the inaccuracy in the fluid description associated with truncation error in the drive-point displacement is reduced.

4.3 Radiated Energy

In order to investigate the effect of the structural discontinuities on the acoustic far-fields, the acoustic intensity distribution is determined for both fluid media. By constructing and examining the acoustic intensity [12, p.64], the redistribution of the radiated energy resulting from the presence of the structural discontinuities can be visualized. The spatially averaged intensity distributions radiating away from the structure for both the top fluid I_1 and the bottom fluid I_2 are normalized to the spatially averaged incident intensity normal to the structure, defined in Eqn.2.23a. This scaling facilitates a simple metric for ensuring that the energetics of the system are properly accounted for and the total outgoing energy is equal in magnitude to the energy incident on the structure. Using Eqns. 4.2, the incident and outgoing

intensities are defined as

$$I_1 = \frac{\langle \langle Re\left[p_1\right] Re\left[v_1\right] \rangle_t \rangle_x}{I_{incident}}, \quad I_2 = \frac{\langle \langle Re\left[p_2\right] Re\left[v_2\right] \rangle_t \rangle_x}{I_{incident}} \tag{4.3}$$

The velocities v_1 and v_2 are the vertical components of the velocity vector field determined from the acoustic momentum equation; this ensures that the outgoing intensities being considered are the components normal to the structure. As a result of orthogonality [15, p.63], none of the cross-modes produced by the multiplication of the real pressure and real velocity expressions contribute to the spatially averaged intensities. The resulting descriptions of the intensity distributions in both fluid media are

$$I_1 = |R|^2 + 2|R||P_{D1,0}| \cos\left(\phi_R - \phi_{D1,0}\right) + \sum_{m_{rad1}} \frac{k_{y1,m}}{k_{y1}} |P_{D1,m}|^2 \tag{4.4a}$$

$$I_2 = \frac{k_{y2}\ \varepsilon_1}{k_{y1}\ \varepsilon_2} \left(|T|^2 + 2|T||P_{D2,0}| \cos\left(\phi_T - \phi_{D2,0}\right) + \sum_{m_{rad2}} \frac{k_{y2,m}}{k_{y2}} |P_{D2,m}|^2 \right) \tag{4.4b}$$

4.3.1 Interpreting Intensity Expressions

In Section 2.4.2 the intensity in the fluid domains as a result of the Unconstrained Membrane motion was considered. Those intensity expressions appear as the first terms in both equations of Eqns. 4.4, and are followed by the effect of the scaled Driven Membrane. The effect of the Driven Membrane is to redistribute the radiated energy to a finite spectrum of angles which is conveyed in the sum over the propagating modes. The middle term in both intensity expressions serves as the mechanism that allows the energy to remain balanced with the introduction of the Driven Membrane intensity contributions. This term takes into account the phase difference between the intensity due to the Unconstrained Membrane and that due to the Driven Membrane at the primary angles, which is the $m = 0$ mode for the

Driven Membrane. As a general physical interpretation, this "cross term" reduces the magnitude of the intensity at the primary angles, and consequently this difference in energy is equivalent to the total energy that is in the redistribution spectrum.

4.4 Sample Intensity Distributions

The resulting intensity distributions in the fluid media determined from Eqns. 4.4 for the fluid and structure parameters used thus far are presented in Figure 4.3 below. The primary angles of reflection and transmission, which are $\theta_r = \theta_t = \pi/4$ because the fluids are identical, are indicated with red markers. In blue are the angles of redistribution resulting from the Driven Membrane radiation.

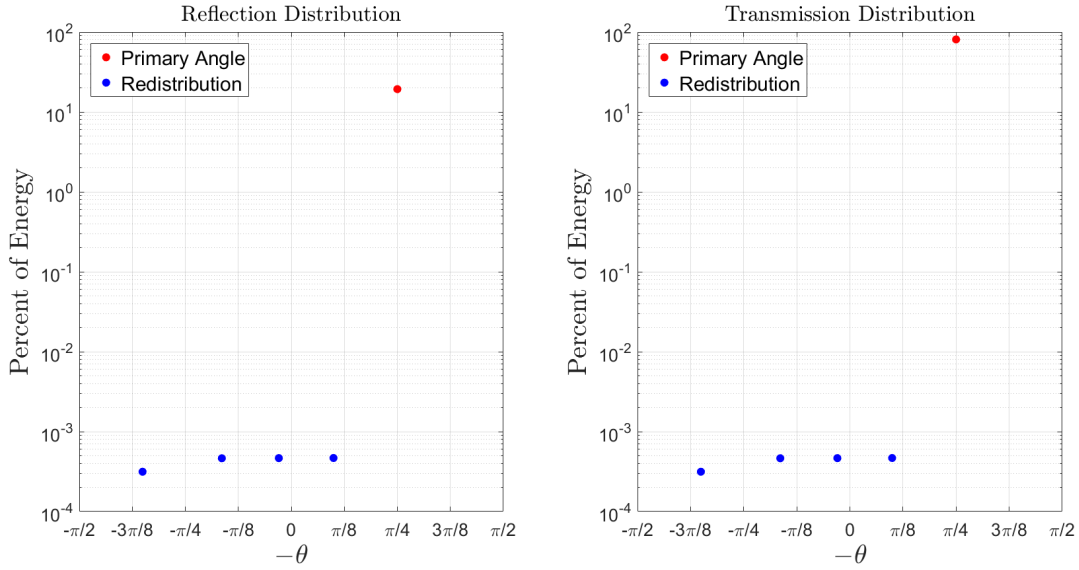

FIGURE 4.3: Intensity Distribution for sample problem. Distributions for (Left) top fluid and (Right) bottom fluid vs radiating angles

These intensity distributions are plotted as percents of the incident energy normal to the structure. Several noteworthy characteristics can be observed from these simple plots. The first is that the redistribution content in both fluids is equivalent, which is a result of the fluids being identical. It also confirms that there are finite number of radiating modes, which in this case is only four modes in addition to

the primary angle. The limited number of modes is a direct outcome of the low frequency considered in this example ($k_1 = 15.7$); as predicted by Eqn. 3.38, as frequency increases so does the number of modes that result in wave propagation. Finally, these plots show that the majority of the energy stays in the primary angles; where the Unconstrained Membrane with these parameter values results in over 80% of the energy transmitted to the fluid domain below the structure. Only a minimal amount of energy is redistributed to other angles: about 0.003% of the energy is reallocated. The lack of energy in the secondary radiating modes suggests that the influence of the Driven Membrane motion and resultant radiating pressures is negligible at this frequency. Recognizing that the Driven Membrane will experience the greatest amplitude in structural motion and radiation at its resonant frequencies, the driving frequency motion is adjusted to excite the nearest resonance and examine the structure behavior.

At this point it is appropriate to note that the frequency of $k_1 = 15.7 \approx 5\pi$ has been used thus far because it was calculated to be one of the resonances of the analogous in-vacuo membrane. However, the resonances predicted by this "dry" configuration do not account for the effect that the fluid loading has on the structural resonances. Corrections to better approximate the resonances of the fluid-loaded membrane are developed in Chapter 5. For now it is simply stated that $k_1 = 16.2$ is a resonance of the system, and the resulting intensity distribution are examined in Figure 4.4. The intensity distribution for a driving frequency of $k_1 = 16.2$ is indicated by the circular markers, while the asterisk replicates the distribution of Figure 4.3.

This plot clearly emphasizes that the extent of energy redistribution to the secondary radiating modes is considerably more significant at resonance, with over 31% of the incident energy being scattered in the configuration above. As expected, the percent of energy at the primary angles must be appropriately reduced to allow for the conservation of energy as predicted in Section 4.3.1.

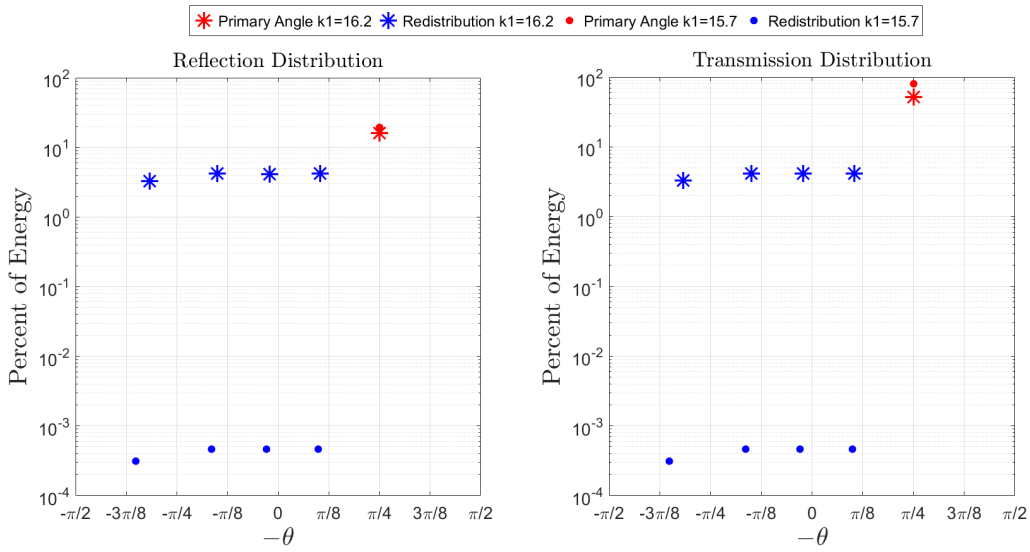

FIGURE 4.4: Intensity Distribution for sample problem off and near resonance. Distributions for (Left) top fluid and (Right) bottom fluid vs radiating angles

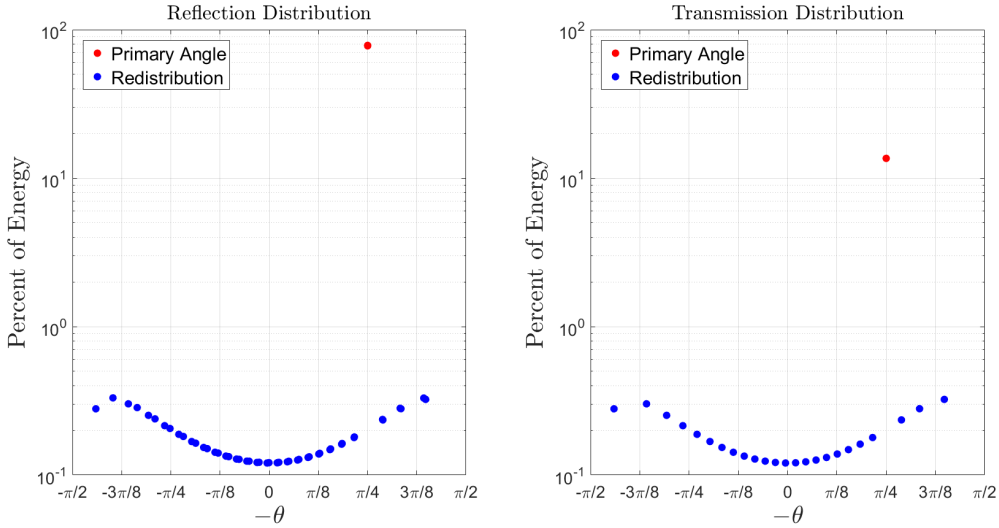

FIGURE 4.5: Intensity Distribution for sample problem at higher resonant frequency. Distributions for (Left) top fluid and (Right) bottom fluid vs radiating angles

As previously established, increasing the driving frequency allows' for an increase in the number of radiating modes and therefore the number of angles within the radiating spectrum. For Figure 4.5, the driving frequency is increased to $k_1 = 78.09$ which is near a resonance of the fluid-loaded structure and is within the third-octave

band centered at $k_c = 80$, which will be the frequency band considered for the remainder of this work. This figure corroborates that increasing the frequency also increases the number of radiating modes. It also reaffirms that for identical fluids, the secondary radiating modes are identical, and the difference in the primary angles is attributed to the reflection and transmission intensity of the Unconstrained Membrane. In this case, the percent of total energy redistributed to angles other than the primary angles is 8.6%, suggesting that the relative re-distribution decreases with frequency. It is believed that this decrease in redistribution is a result of the decrease in displacement amplitude of the Unconstrained Membrane with frequency. This in turn decreases the amplitude of the Driven Membrane motion and ensuing radiated pressures by way of the scaling factor λ.

Instead of investigating the energy redistribution a single frequency at a time, it is advantageous to calculate the percent of energy redistributed as a function of frequency. In Figure 4.6 the percent of power redistributed to angles other than the primary angles is plotted for the third-octave band centered at $k_c = 80$.

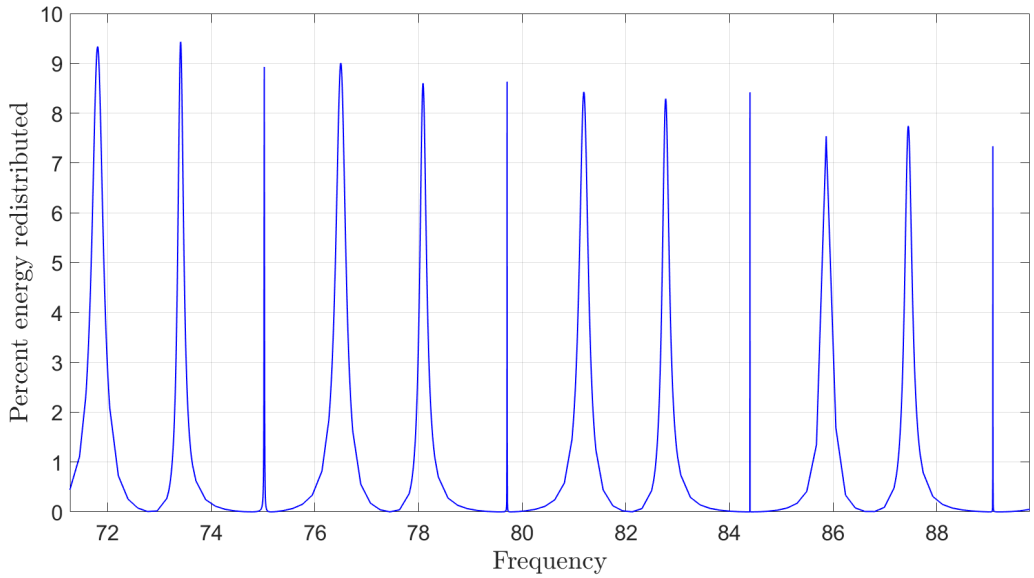

FIGURE 4.6: Percent of energy redistributed to radiation angles other than the primary angle

This distribution of power supports the statement that the percent of incident power re-distributed to the secondary radiating modes decreases with increasing frequency. The most striking characteristic of this distribution is that it seems that every third peak is exceedingly sharp, relative to the rest. It is proposed and verified in the first couple of sections in Chapter 5 that this variability in peak width is a result of destructive interference of the structural reverberation caused by the phase-difference between the drive-points' forcing.

It is interesting to briefly return to the analysis of Section 3.6.2 to consider the convergence rates at a driving frequency near a structural resonance. The convergence analysis performed in Section 3.6.2 was for a low frequency that was demonstrated to be off-resonance. In Figure 4.7 below, the drive-point convergence of the Driven Membrane at the current frequency of interest $k_1 = 78.08$ is depicted.

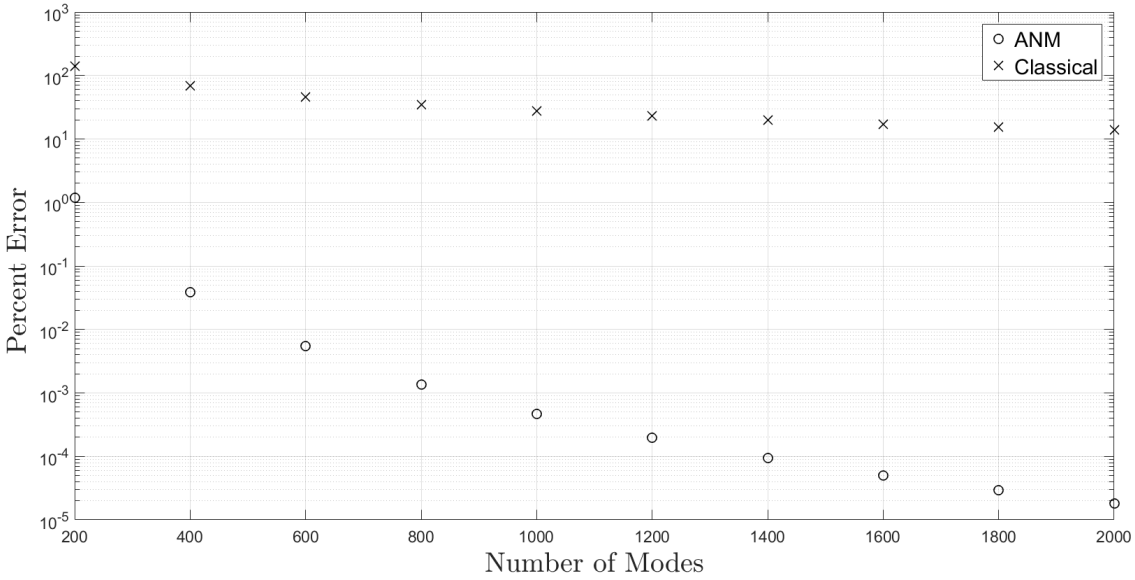

FIGURE 4.7: Convergence of structural displacement at drive point for Driven Membrane at $k_1 = 78.09$; Classical and ANM Solutions

As expected, a higher driving frequency increases the number of modes necessary for an accurate description of the quickly oscillating structure. The convergence rate

is slower for both the ANM and Classical methods for a higher frequency. It does not appear that driving the system near resonance contributes to the slower convergence of drive-point displacement. However, it is crucial to recognize that at resonance, the amplitude of the motion along the length of the structure is large, and since the Driven Membrane is inversely scaled to the relatively small drive-point displacement, any error resulting from the convergence of the drive-point description becomes more significant in the assembly of the Periodically Fixed Membrane response [1].

5

Finite Baffled Structure

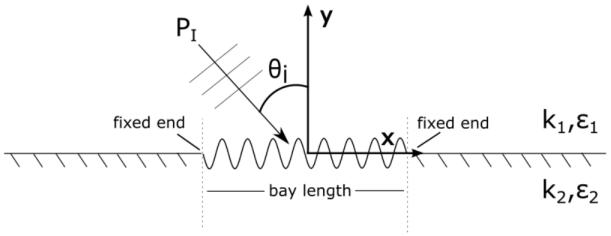

FIGURE 5.1: Fluid-loaded finite membrane in an infinite baffle driven with an obliquely incident acoustic wave

In this chapter, the treatment of a finite membrane in an infinite baffle is presented. The objective is to model the response of the membrane and coupled fluid media to an acoustic wave obliquely incident on the structure. This geometry is designed to represent one bay of the Periodically Fixed infinite membrane. However, it is convenient to place the origin at the midpoint between the two constraints in the case of the finite model. The goal for this work is to motivate the development of simple closed form directivity patterns and validate them using the infinite structure established in the previous chapter.

Formally including the complete effect of the fluids is mathematically difficult as a

result of the finite nature of the membrane and the resulting hydrodynamics near the edges of the structure. Therefore, the analysis begins with "zeroth-order" approximation of the in-vacuo motion of a finite membrane. In order to begin to introduce the effects of the fluid loading, a first-order inertance and damping approximation are introduced and evaluated. This finite model will be assembled similar to the infinite Periodically Fixed Membrane of Chapter 4. The motion of a finite membrane driven at the end-points, referred to as the "Forced-Forced Membrane", will be scaled to the motion of a segment of the Unconstrained Membrane in order to bring the end-points of the finite structure to rest. As with the Driven Membrane in Chapter 3, the discrete forcing on the Forced-Forced Membrane will include a phase difference in the forcing. Figure 5.1 depicts the two components used to assemble the model for the acoustically driven finite membrane with fixed end-points, centered at the origin.

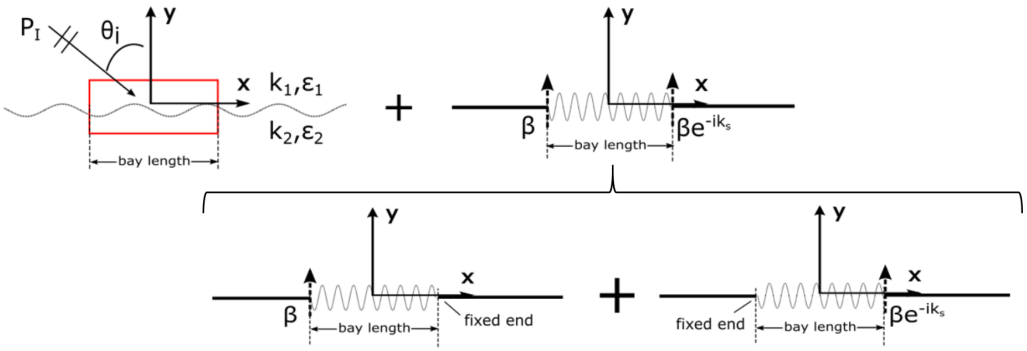

FIGURE 5.2: Left: the red box represents the segment of the Unconstrained Membrane used in modeling the finite membrane. Right: the configuration of the in-vacuo Forced-Forced Membrane, and its components described by η_{ff_1} and η_{ff_2}

5.1 In-Vacuo Membrane Model

The Unconstrained Membrane was developed in detail in Chapter 2. The in-vacuo model for the Forced-Forced Membrane is solved using the governing equation of the membrane and applying the boundary conditions. The in-vacuo model can be

interpreted as an approximation to the motion of the membrane surrounded by light-weight fluids of negligible effect on the membrane dynamics. The motion at the end-point is assumed to be time-harmonic. The problem is treated using superposition, where one component is driven on the left boundary and fixed on the right and is described by η_{ff_1}, and the second component has the left end fixed and the right end driven to describe η_{ff_2}, as shown in Figure 5.2. The governing equation and boundary conditions described are

$$-\eta'' - k_M^2 \eta = 0 \tag{5.1}$$

$$\eta_{ff_1}(-\tfrac{1}{2}) = \beta \qquad \eta_{ff_2}(-\tfrac{1}{2}) = 0$$

$$\eta_{ff_1}(\tfrac{1}{2}) = 0 \qquad \eta_{ff_2}(\tfrac{1}{2}) = \beta e^{-ik_s}$$

where β is the prescribed complex displacement amplitude. The resultant motion due to the end-point driving is

$$\eta_{ff} = \eta_{ff_1} + \eta_{ff_2} = \frac{\beta}{\sin(k_M)}\left[\sin\left(k_M(-x+1/2)\right) + e^{-ik_s}\sin\left(k_M(x+1/2)\right)\right] \tag{5.2}$$

It will be shown in the coming sections that it is convenient to work with the spatially averaged mean-square velocity of the structure; this parameter is expressed as

$$\left\langle \bar{V} \right\rangle_x^2 = \frac{k_1^2|\beta|^2}{2}\left(\frac{\cos k_s - \cos k_M}{k_M \sin k_M} + \frac{1 - \cos k_M \cos k_s}{\sin^2 k_M}\right) \tag{5.3}$$

From these expressions it is evident that the membrane motion exhibits resonant behavior at certain frequencies and the motion becomes unbounded. The set of structural wavenumbers

$$k_M^* = n\pi, n \in \mathbb{Z} \tag{5.4}$$

includes all of the possible resonances, but the phase difference between the prescribed displacements k_s defines the effective set of resonances for the given parameters. For example, if the normal incidence case is being considered, there is no

phase difference between the end-point displacements ($k_s = 0$), and the structural resonances occur at $k_M^* = m\pi$ where m is an odd integer. This represents the physical phenomenon that depending on the phase difference between the prescribed drive-point displacements of the two membrane motions η_{ff_1} and η_{ff_2}, there may be destructive interference that will reduce, or exactly cancel, the significance of the resonances.

In order to explore this phenomenon further, and to introduce models to the in-vacuo description that will begin to approximate the effect of the surrounding fluid media, a small dissipative component is introduced into the structural wavenumber.

5.2 Membrane on a Viscous Suspension

One of the effects of the fluid loading is to act as a resistive force and oppose the motion of the structure [8, p.57]. In Section 2.4.1 it was suggested that the fluid loading can be partially interpreted as a frequency-dependent damping. This motivates adapting the model of the in-vacuo membrane by effectively placing the membrane on a continuous damper suspension of strength per unit length $\bar{R}$, so that the governing equation of the membrane motion and the boundary conditions are [11, p.171]

$$-\frac{\partial^2 \eta}{\partial x^2} + ik_1\bar{R}\eta - k_M^2\eta = 0 \tag{5.5}$$

$$\eta(-\tfrac{1}{2}) = \beta, \quad \eta(\tfrac{1}{2}) = \beta e^{-ik_s}$$

The damper proportional to transverse velocity will dissipate energy from the system, which represents the energy radiated through the fluid media. The damper, like the fluid loading, will bound the motion of the membrane at the structural resonances. Currently no information about the value of the damper is known, other than it is frequency-dependent. The process of choosing the damper value requires

matching the power dissipated by this system to the power radiated by an analogous configuration. This argument and process are presented in the following sections.

The dispersion relation defines the structural wavenumber that is used in the solution to the damped membrane motion, which is

$$\gamma = \sqrt{k_M^2 - ik_1\bar{R}} \tag{5.6a}$$

$$\eta_{ff_R} = \frac{\beta}{\sin(\gamma)}\left[\sin(\gamma(-x+1/2)) + e^{-ik_s}\sin(\gamma(x+1/2)\right] \tag{5.6b}$$

At this point, the assumption of small damping relative to the in-vacuo structural wave number is introduced. This justifies the use of a Taylor Series expansion around a zero damper value to begin approximating the effect of the damper. The first term of the Taylor Series for small damping is calculated for the structural wavenumber and the membrane motion to produce

$$\gamma \approx k_M - i\frac{M_1}{2}\bar{R} = k_M - iR \tag{5.7}$$

$$\eta_{ff_R} \approx \frac{\beta}{\sin(k_M - iR)}\left[\sin(k_M(-x+1/2)) + e^{-ik_s}\sin(k_M(x+1/2)\right] \tag{5.8}$$

In Eqn. 5.7 a new parameter $R = M_1\bar{R}/2$ is introduced for conciseness. It is found that to first order, the small damping does not affect the mode shape of the motion. It does, however, introduce a complex component to the denominator, as compared to Eqn. 5.2, which will bound the amplitude of the motion at resonance. The spatial average of the damped membrane motion mean square velocity is described as

$$\left\langle \bar{V}^2 \right\rangle_x = \frac{k_1^2|\beta|^2}{2k_M}\left(\frac{2\cos(k_s)\left[k_M\cos k_M - \sin k_M\right] + \sin(2k_M) - 2k_M}{\cos(2k_M) - \cosh(2R)}\right) \tag{5.9}$$

The spatial average mean square velocity is of interest because it is proportional to the power dissipated $\mathbb{P}$ by the system by the relationship [8, p.14],

$$\mathbb{P} = \bar{R}\left\langle \bar{V}^2 \right\rangle_x = \frac{2R}{M_1}\left\langle \bar{V}^2 \right\rangle_x \tag{5.10}$$

This is analogous to the power dissipated by a simple damped oscillator. As with the simple harmonic oscillator, the most power will be dissipated at the resonant frequencies. As a result of the small damper approximation, the resonances of the damped structure are initially assumed to be the same as for the in-vacuo configuration. It is further predicted (and will be shown) that the power plotted as a function of frequency will have sharp peaks concentrated at the resonances as a result of the small damping [8, p.15]. Evaluating Eqn. 5.9 at the resonances $k_M^* = n\pi$, the expression reduces to

$$\left\langle \bar{V}^2 \right\rangle_x \Big|_{k_M = k_M^*} = \frac{(n\pi M_1)^2 |\beta|^2}{2R^2} \left(1 - (-1)^n \cos k_s\right) \tag{5.11}$$

In this simplified expression, it is possible to see the effect that the phase difference between the drive-point motions has on determining the extent of destructive interference of the structural waves. This interference can be interpreted as the superposition of the resultant structural waves from the two "driven-pinned" sub-problems (depicted in Figure 5.2) that constitute the Forced-Forced Membrane. Momentarily assuming that within the frequency band of interest the damper value and frequency are slowly varying, the simple result of

$$1 - (-1)^n \cos k_s \tag{5.12}$$

dictates the relative amplitude of the power dissipated at each resonance. This simple expression also predicts which, if any, of the structural wavenumbers defined by Eqn. 5.4 do not result in resonant behavior. That is, if the phase difference k_s is a harmonic of the resonant frequencies $k_s = k_1 \sin\theta = q\pi, q \in \mathbb{Z}$, then there will be natural frequencies where the net motion of the structure will experience exact cancellation. For example, when the end-points are driven in phase $k_s = 0$, the result that only the odd modes result in resonances is reproduced.

In order to predict the appropriate values of the damper to approximate the dissipative effect of the fluids, it is beneficial to first introduce a correction for the inertance effect that the fluids have on the structure. With this effective inertance introduced, the methodology developed for approximating the damper values is presented in Section 5.4.

5.3 Membrane Inertance Correction Model

The objective is to model the effective additional mass per length that the fluid loading enacts on the membrane, and introduce it into the structural wavenumber. To motivate this "inertance correction," the analysis begins with the governing equation for an infinite fluid-loaded membrane in free motion, which is described by Eqn. 2.17 without the external loading term. The resulting dispersion relation for this free membrane can be written in a slightly unconventional form as,

$$k_\chi^2 - k_M^2 \left(\frac{\varepsilon_1}{\sqrt{k_\chi^2 - k_1^2}} + \frac{\varepsilon_2}{\sqrt{k_\chi^2 - k_2^2}} \right) = k_M^2 \tag{5.13}$$

where k_χ is the structural wavenumber. In order to formally solve for the structural wavenumber that includes the inertance contribution of the fluid media, the roots of this high order polynomial would need to be numerically determined. However, since one of the goals stated at the beginning of this chapter was to motivate simple closed form expressions, an approximation is pursued. Examining Eqn. 5.13, it is possible to quickly deduce two initial approximations of k_χ, which are potential starting points for an iterative solution to the dispersion relation. The simplest approximation is the case of no fluid loading, $\varepsilon_1 = \varepsilon_2 = 0$, resulting in

$$k_\chi = k_M \tag{5.14}$$

which reproduces the structural wavenumber of the in-vacuo membrane. The next simplest approximation is that of the fluids being constant density so that

$$k_\chi^2 - k_M^2 \left(\frac{\varepsilon_1}{k_\chi} + \frac{\varepsilon_2}{k_\chi} \right) = k_M^2 \tag{5.15}$$

This approximation would require solving a cubic equation to determine the first estimate of the iteration scheme. Additionally, some of the roots of this equation would result in complex wavenumbers, so it would be necessary to choose the real root as the first estimate since the resistive influence of the fluid has already been addressed with the viscous suspension model. The initial estimate of no fluid loading $k_{\chi_o} = k_M$ is used because it exactly describes the in-vacuo model that is the basis of our analysis, and the subsequent iterations will result in real wavenumbers. The real wavenumbers ensures that this iterative technique will contribute only an inertance correction to model the fluid loading. The iteration scheme is defined as

$$\bar{k}_{\chi_j} = \frac{k_{\chi_j}}{k_M}, \quad \bar{k}_{\chi_o} = 1 \tag{5.16}$$

$$\bar{k}_{\chi_{j+1}} = \sqrt{1 + \frac{1}{k_M} \left(\frac{\varepsilon_1}{\sqrt{\bar{k}_{\chi_j}^- - M_1^2}} + \frac{\varepsilon_2}{\sqrt{\bar{k}_{\chi_j}^- - M_2^2}} \right)} \tag{5.17}$$

The first four iterations of this scheme are presented in Figure 5.3 over the third-octave band centered at $k_c = 80$ for the parameter values used throughout this thesis. This figure illustrates that the inertance correction increases the structural wavenumber of the membrane, which results in decreasing the resonant frequencies of the system as compared to the in-vacuo configuration.

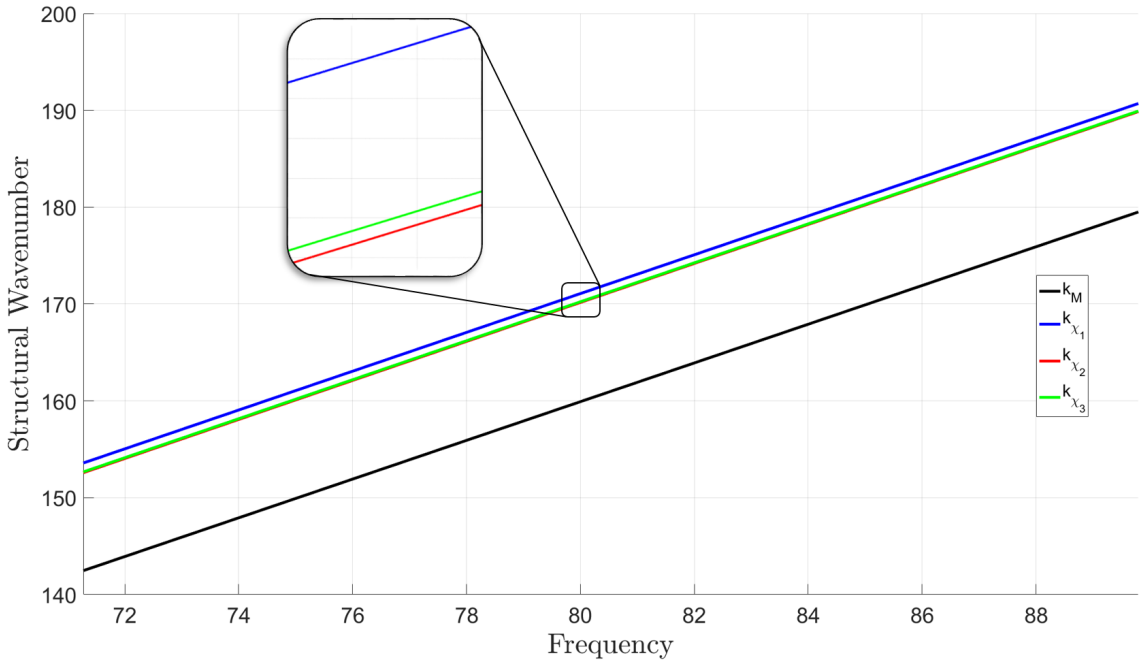

FIGURE 5.3: Convergence of inertance iterative model: first four iterations shown

The figure also suggests that the iterations quickly converge for the parameters used in this investigation. As the Mach numbers increase, the iterations converge more slowly. In order to qualify the convergence of the iterations, the percent error of the first six iterations are plotted in Figure 5.4. This error is calculated relative to an iterated solution that was converged to an accuracy well beyond the error associated with these first couple of iterations. The percent error presented is frequency averaged over the third-octave band centered at $k_c = 80$[1]. The quick convergence of this iterative model, suggested by the previous two plots, justifies using the first iteration as an initial approximation for the inertance of the fluids affecting the structural wavenumber.

[1] An alternative approach could have been to evaluate the percent error at the center frequency. Since the modified structural wavenumber k_χ is approximately linear with frequency (as shown in Figure 5.3), there is negligible variation in error with frequency.

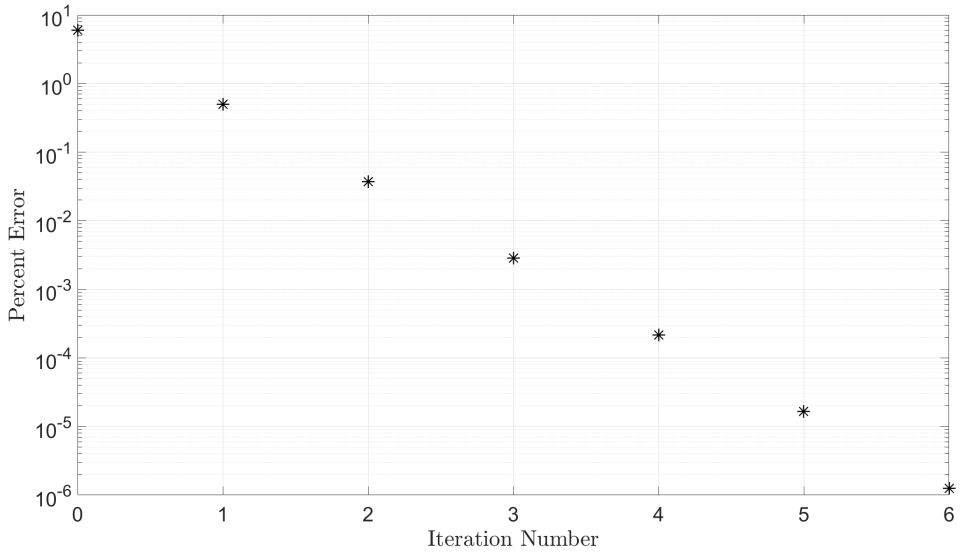

FIGURE 5.4: Convergence of inertance iterative model: Frequency averaged for third-octave band centered at $k_c = 80$

The modified wavenumber due to this first iteration is

$$k_{\chi_1} = k_M \sqrt{1 + \frac{1}{k_M}\left(\frac{\varepsilon_1}{\sqrt{1-M_1^2}} + \frac{\varepsilon_2}{\sqrt{1-M_2^2}}\right)} \tag{5.18}$$

In practice, application of this modified structural wavenumber k_χ is as simple as replacing the in-vacuo wavenumber $k_M \rightarrow k_\chi$ in the governing equation. One way to illustrate the effect of this fluid inertance correction is to compare the resultant motion of the finite membrane to the motion over one bay of the fluid-loaded Periodically Fixed Membrane assembled in Chapter 4. In order to compare these models, the finite membrane must be brought to rest at the end-points by scaling and superposition of the Unconstrained Membrane segment, as outlined in Figure 5.2. Additionally, a simple variable transformation in x is introduced in the finite model to translate the constraint locations to match those of the Periodically Fixed Membrane (at integer values of x). The real motion of the in-vacuo membrane with and without the first iteration of the inertance correction in the structural wavenumber is plotted against that of the fluid-load infinite membrane in Figure 5.5. The

parameter values of this configuration are those used throughout this analysis, and the driving frequency is $k_c = 80$.

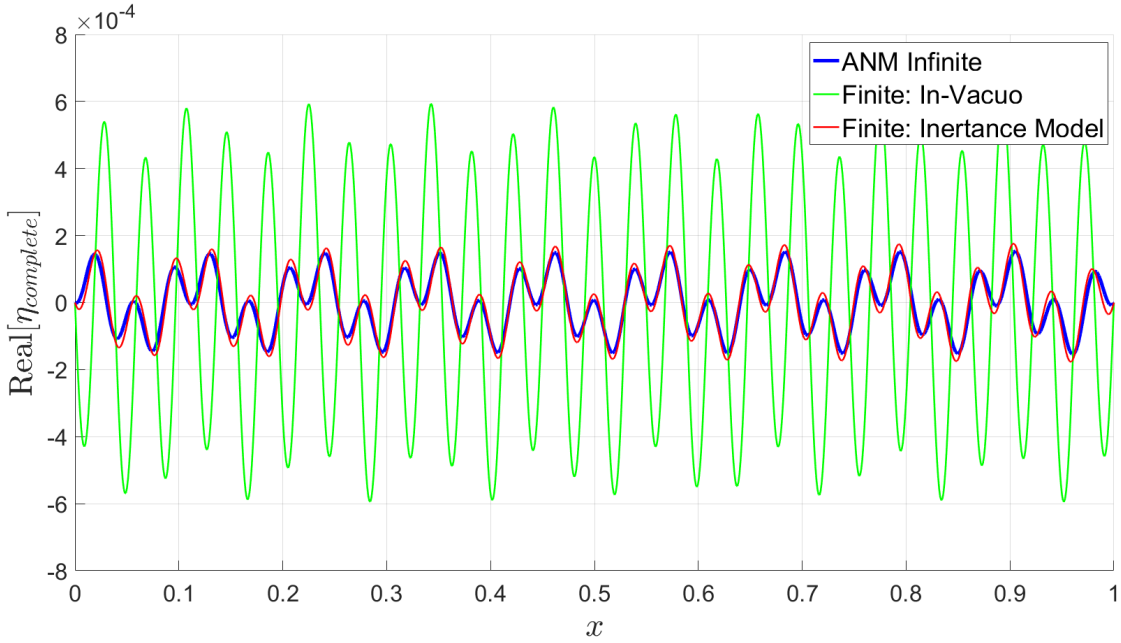

FIGURE 5.5: Comparison of membrane motion determined from the fluid-loaded infinite membrane (one bay), and the finite membrane with and without the inertance correction

Figure 5.5 clearly demonstrates that the motion of the in-vacuo membrane is altered with the introduction of the inertance model. The agreement between the motion of fluid-loaded membrane and the finite model with just the first iteration of the inertance correction is impressive. As expected, all three models have zero displacement at $x = 0$ and $x = 1$ as defined by the fixed constraints.

Combining both of the fluid effect models just developed (damping and additional inertance) in the finite-structure model is done by modifying the membrane motion on the viscous suspension Eqn. 5.8 to include the inertance correction as

$$\eta_{ff_{R,I}} \approx \frac{\beta}{\sin\left(k_{\chi_1} - iR\right)} \left[\sin\left(k_{\chi_1}(-x + 1/2)\right) + e^{-ik_s} \sin\left(k_{\chi_1}(x + 1/2)\right)\right] \tag{5.19}$$

5.4 Power Matching

With a model of the membrane motion including corrections to approximate the effects of the fluid, it is now possible to calculate the damper values necessary to equate the power dissipated by this system to the total power radiated by the original fluid-loaded finite membrane independent of the viscous suspension.

5.4.1 Radiated Power using Rayleigh Integral

The power radiated by the end-driven finite membrane is evaluated using the two-dimensional Rayleigh Integral. The Rayleigh Integral allows for the calculation of fluid pressures from the normal vibration of a planar surface that is infinitely baffled. Although the two-dimensional formulation is not as readily available in most textbooks, the development closely follows that of the three-dimensional description which is presented in most acoustic textbooks [10, p.214], [2, p.59], [12, p.88], [7, p.375]. The 2D Rayleigh Integral is developed from a continuous distribution of two-dimensional monopoles, whose resultant pressure fields are written in terms of Hankel functions of the second kind of order zero. As in the three-dimensional derivation, the strength of the monopoles is related to the vertical velocity of the surface. Since the Rayleigh Integral is evaluated in the far-field (relative to the length of the structure), the Hankel function is rewritten in its asymptotic form

$$H_0^{(2)}(kr) \approx \left(\frac{2}{\pi kr}\right)^{1/2} e^{-i\left(kr-\frac{\pi}{4}\right)} \tag{5.20}$$

and higher order effects are neglected in the amplitude, but not the phase. The resulting far-field pressures from the Rayleigh Integral for the two fluid spaces above and below the structure are, respectively,

$$p_1(r,\phi_1) = \frac{\varepsilon_1}{M_1^2}\left(\frac{k_1}{2\pi r}\right)^{1/2} e^{i(k_1 t - k_1 r + \pi/4)} \int_{-1/2}^{1/2} V(x) e^{-ik_1 x \sin\phi_1} dx \tag{5.21a}$$

$$p_2(r,\phi_2) = \frac{\varepsilon_2}{M_1 M_2}\left(\frac{k_2}{2\pi r}\right)^{1/2} e^{i(k_1 t - k_2 r + \pi/4)} \int_{-1/2}^{1/2} V(x) e^{-ik_2 x \sin\phi_2} dx \tag{5.21b}$$

where ϕ is the angle of radiation and $V(x)$ is the transverse velocity of the surface, which in the current investigation is that of the finite membrane denoted as

$$V(x) = ik_i\eta = V_o\left[\sin\left(k_\chi(-x+1/2)\right) + e^{-ik_s}\sin\left(k_\chi(x+1/2)\right]\right. \tag{5.22}$$

In this analysis, it is assumed that the amplitude of the velocity V_o is known. It will be shown in the next section that the same finite amplitude is assumed for the motion of the membrane on a suspension, and because of linearity does not affect the value of the required damper. The integrals in Eqns. 5.21 are analytically evaluated. In this section only the power radiated into the top fluid is presented as the power radiated to the bottom fluid follows the same analysis. Applying the assumption that in the far-field the relationship between the acoustic pressure and velocity is that of a plane wave [12, p.65], the acoustic intensity is immediately stated as a function of the pressure amplitude squared and the planar acoustic impedance

$$I_1(\phi_1) = \frac{|p_1|^2}{2\cdot(\varepsilon_1/M_1)} \tag{5.23}$$

The intensity distribution for the top fluid is therefore defined as

$$I_1(\phi_1) = \frac{k_1|V_o|^2\varepsilon_1}{\pi M_1 r}\ D(\phi_1) \tag{5.24}$$

$$D(\phi_1) = \left(\frac{\sin\left(\frac{1}{2}(k_\chi - k_s)\right)\sin\left(\frac{1}{2}(k_\chi - k_1\sin\phi_1)\right)}{k_\chi - k_1\sin\phi_1}\right. \tag{5.25}$$

$$\left. + \frac{\sin\left(\frac{1}{2}(k_\chi + k_s)\right)\sin\left(\frac{1}{2}(k_\chi + k_1\sin\phi_1)\right)}{k_\chi + k_1\sin\phi_1}\right)^2$$

where $D(\phi_1)$ is the directivity function. As expected for a two-dimensional configuration, the acoustic intensity is inversely proportional to the distance from the

source. The acoustic power $\mathbb{P}_{Rad1}$ is evaluated by performing a surface integral over a semi-circle in the far-field centered at the origin so that

$$\mathbb{P}_{Rad1} = \int_{-\pi/2}^{\pi/2} I_1 \; r d\phi_1 \tag{5.26}$$

This surface is particularly convenient because the intensity distribution described in Eqn. 5.24 is the radial component of the intensity, which is defined as being normal to a semi-circle surface.

5.4.2 High Frequency Approximation

At this point, the analysis is restricted to the high frequency region. This high frequency assumption allows the directivity function $D(\phi_1)$ of the intensity distribution to be approximated as

$$D(\phi_1) \approx \left(\frac{\sin^2\left(\frac{1}{2}(k_\chi - k_s)\right)}{2(k_\chi - k_1 \sin\phi_1)^2} + \frac{\sin^2\left(\frac{1}{2}(k_s + k_\chi)\right)}{2(k_\chi + k_1 \sin\phi_1)^2} \right. \tag{5.27}$$
$$\left. - \frac{\cos(k_\chi)\sin\left(\frac{1}{2}(k_s + k_\chi)\right)\sin\left(\frac{1}{2}(k_\chi - k_s)\right)}{(k_\chi - k_1 \sin\phi_1)(k_\chi + k_1 \sin\phi_1)} \right)$$

The exact and high frequency approximation of the directivity function are plotted in Figure 5.6 below for a frequency of k=80.

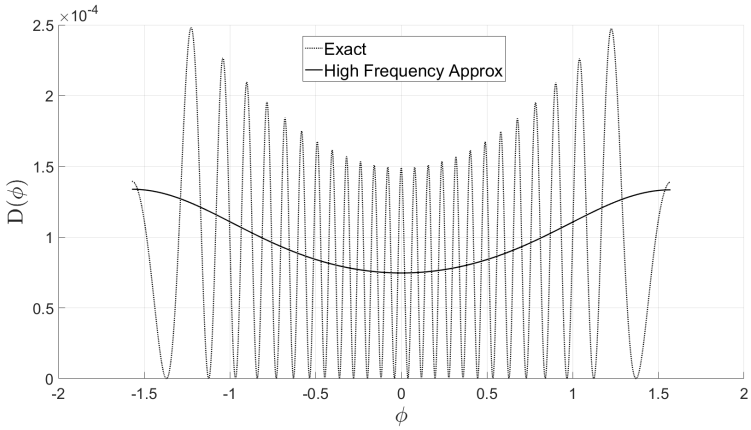

FIGURE 5.6: Acoustic intensity distribution and high frequency approximation

This high frequency assumption approximately averages the highly oscillatory behavior of the directivity function, thereby allowing for a closed-form evaluation of the surface integral to determine the total power radiated. Evaluating Eqn. 5.26 using the asymptotic directivity function, the power radiated into the top fluid is approximated by the simple closed form expression[2]

$$\mathbb{P}_{Rad1} = -\frac{k_1|V_o|^2\varepsilon_1\left(k_1^2 - 3k_\chi^2 - 2\left(k_1^2 - 2k_\chi^2\right)\cos(k_\chi)\cos(k_s) + \left(k_1^2 - k_\chi^2\right)\cos(2k_\chi)\right)}{4k_\chi M_1\left(k_\chi^2 - k_1^2\right)^{3/2}} \tag{5.28}$$

An expression for the power radiated into the bottom fluid $\mathbb{P}_{Rad2}$ is similarly determined using the corresponding fluid properties.

5.4.3 Power Matching to Determine Damper Value

The total power radiated by the membrane motion stated in Eqn. 5.22 is found by adding the power radiated into both fluid media. The power dissipated by the membrane on a suspension $\mathbb{P}_d$ with the same velocity amplitude V_o is determined by Eqn. 5.10 where $\left\langle \bar{V}^2 \right\rangle_x$ is the spatial average of the mean square velocity of Eqn. 5.22. Equating the total power dissipated by both configurations,

$$\mathbb{P}_d = \mathbb{P}_{Rad1} + \mathbb{P}_{Rad2} \tag{5.29}$$

an algebraic expression, independent of the velocity amplitude V_o, for the frequency-dependent damper necessary to satisfy this condition is immediately determined as

$$R = \frac{\mathbb{P}_{Rad1} + \mathbb{P}_{Rad2}}{\frac{M_1}{2}\left\langle \bar{V}^2 \right\rangle_x} \tag{5.30}$$

The damper function calculated as a function of frequency using the characteristic fluid and structure parameters used throughout this analysis is plotted in Figure 5.7 below.

[2] For the characteristic parameters used in Figure 5.6, the high frequency approximation results in a calculated power that is about 9% larger than the exact power (numerically integrated).

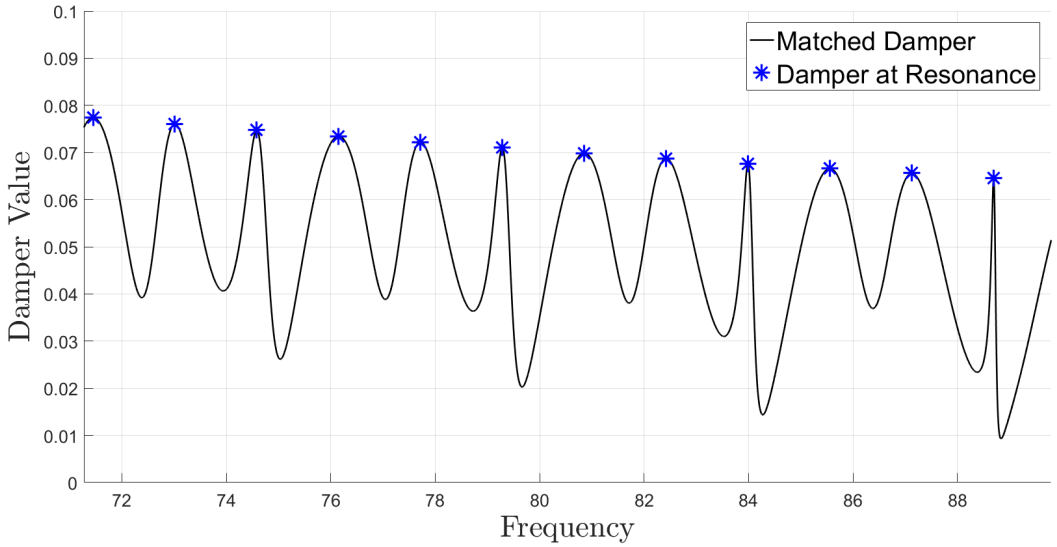

FIGURE 5.7: Calculated damper values from power-matching

In the figure above, the damper values calculated at the resonant frequencies of the system are denoted by a blue marker. As expected, the damper value is largest at these frequencies where the stiffness and inertial effects balance and the membrane experiences the most motion, and therefore results in the most radiation into the fluids. The power dissipated by the membrane on a suspension with the damper values calculated, and by definition also the power radiated by the analogous membrane, is shown in Figure 5.8.

The drive-point displacement is prescribed to be the same constant for all frequencies in determining the power in the figure above. It is confirmed that the system dissipates the most power at the resonances, and the power peaks as a function of frequency are sharp, which motivates the frequency perturbation analysis pursued in Section 5.5.

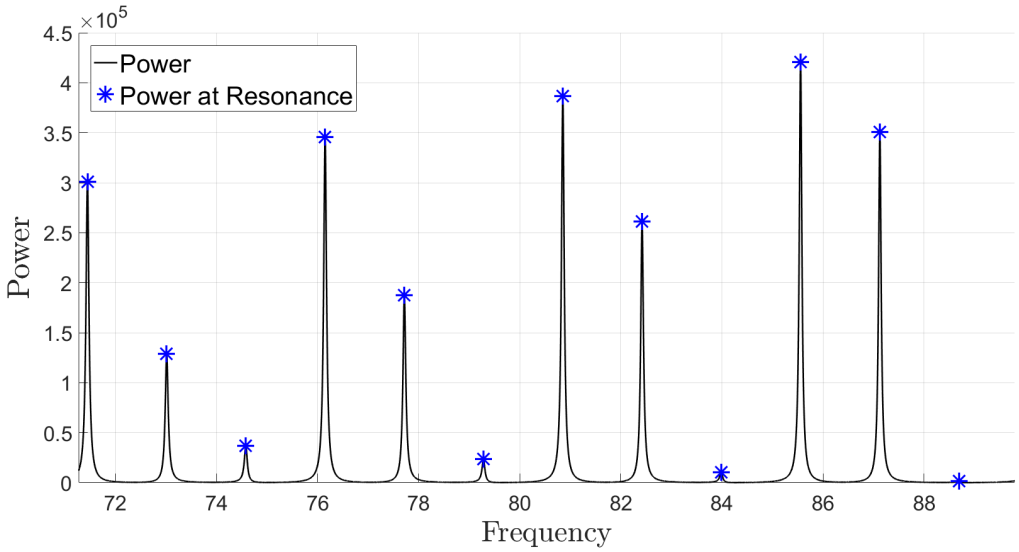

FIGURE 5.8: Power dissipated from calculated damper value. Equivalent to power radiated

5.4.4 Damper Functional Dependence

In order to better visualize the trends of the damper and the corresponding power calculated as a function of frequency, Figures 5.7 and 5.8 are reproduced over a larger frequency range below.

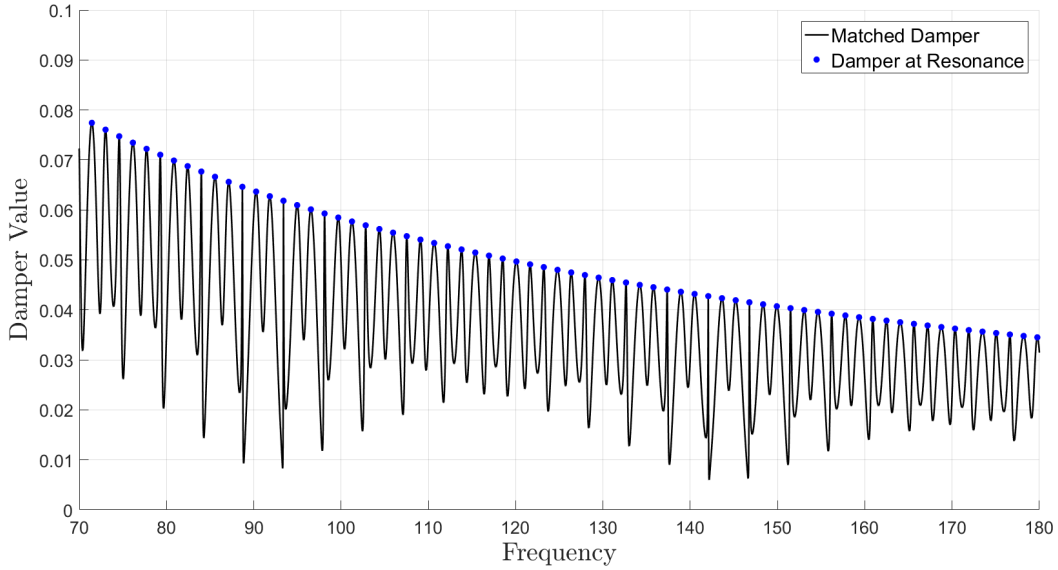

FIGURE 5.9: Calculated damper values from power-matching

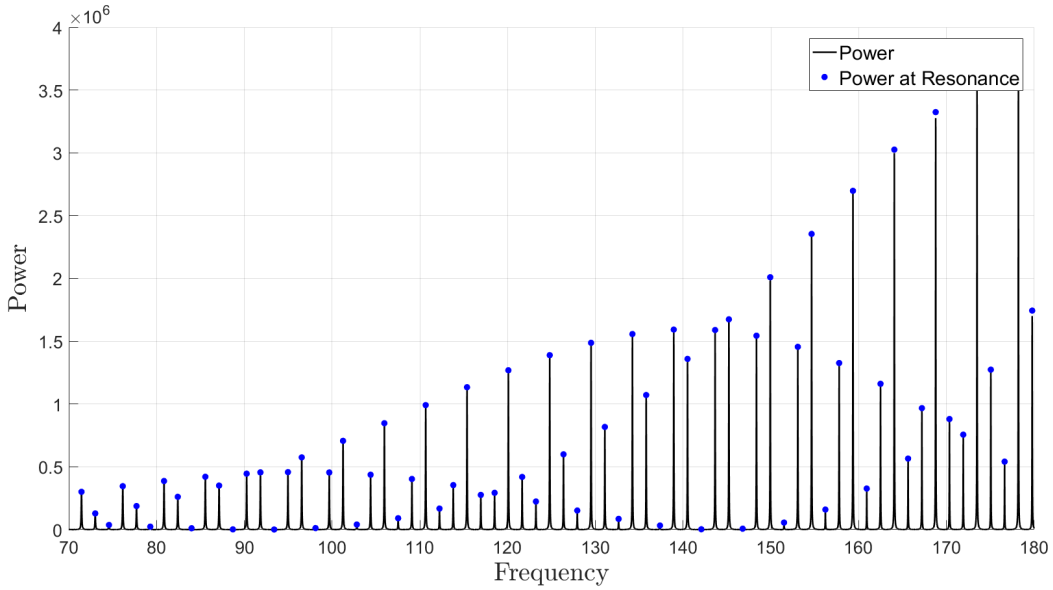

FIGURE 5.10: Power dissipated from calculated damper value. Equivalent to power radiated

These plots show that the damper value is inversely proportional to frequency, and the power radiated oscillates with frequency with an overall envelope that increases with frequency. Careful examination of the expression for the power radiated into the top fluid Eqn. 5.28 shows that the power is proportional to k_1^3 to leading order. This proportionality is a result of the membrane velocity definition V_o as a function of a constant drive-point displacement β independent of frequency, so that

$$V_o = \frac{ik_1\beta}{\sin\left(k_{\chi_1} - iR\right)} \tag{5.31}$$

In Chapter 6, it is shown that the power's frequency dependence is dominated by the definition of the drive-point motion. The oscillation in power within this envelope is explained by the destructive interference resulting from the drive-point phase difference described in Section 5.2. It is beneficial to refer back to Figure 5.8 since within this third-octave band the effect of the k_1^3-envelope is not as dominant. In this figure, the relative amplitudes of the peaks are primarily explained by the extent of destructive interference that affects the average mean-square velocity of the

structure, and therefore the power dissipated/radiated.

In order to understand the decreasing damper value with frequency, it is advantageous to first interpret the power radiated in the framework of the edge radiator results developed by Bliss [16].

In this work, Bliss demonstrates that the directivity of the radiation from a finite subsonic panel is explained in terms of higher order singularities at the edges, and is not predicted by uncanceled edge monopoles [17]. As the driving frequency increases, the membrane structural wavenumber increases, thereby decreasing the structural wavelength. The strength[3] of the edge radiators is proportional to this structural wavelength, with the high order singularities (dipole, quadrapole, etc) decreasing in strength faster than the monopole. The coupling between structure and fluid is reduced with smaller edge sources. As the frequency increases the strength of the edge radiators decrease, however, the active length of the damping suspension does not change with frequency; the length of the membrane on the viscous suspension is constant. Therefore, in order for the distributed damping to match the power of the diminishing edge radiators, the strength of the damper must decrease. Recall that the damper value is independent of the velocity amplitude V_o (Section 5.4.3), so the damper frequency dependence is independent of the power frequency dependence.

5.5 Frequency Expansion Analysis

The plots of power as a function of frequency in the previous section confirm the assumption made in Section 5.2 that the peaks around the resonances would be sharp as a result of the small damping approximation. This behavior suggests that a perturbation analysis with respect to frequency may be a valid approach for predicting the half-power width of the resonance peaks.

[3] Perhaps a more intuitive physical interpretation is that the "size" of the edge radiators decrease with increasing frequency

The purpose of this perturbation analysis is to define the half-power width for each resonance peak in order to be able to predict the total power dissipated over the frequency band of interest. It was already shown that it is possible to predict the power at the resonance and the location of the resonances. With information about the half-power width, it is then possible to estimate the total dissipated power within a frequency band, such as the third-octave band centered at $k_c = 80$ in Figure 5.8.

In order to establish the half-power width, it is necessary to determine the frequencies on either side of the resonance that correspond to a power dissipated equal to half of the power at the known resonant frequency. The half-power frequency on the lower side of resonance is termed $k_{-\delta}$, and the half-power frequency on the other side of the resonance peak is termed $k_{+\delta}$. These parameters are illustrated in Figure 5.11 below.

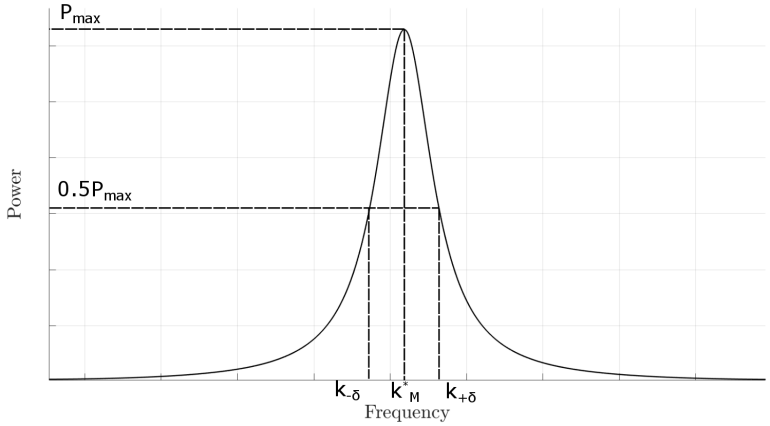

FIGURE 5.11: Definition of half power and the lower $k_{-\delta}$ and upper $k_{+\delta}$ perturbed frequencies

The approach of the perturbation analysis assumes that the half power frequencies can be written with a small parameter δ as

$$k_{-\delta} = k_M^* - \delta = n\pi - \delta \tag{5.32}$$

$$k_{+\delta} = k_M^* + \delta = n\pi + \delta \tag{5.33}$$

The following analysis will be presented for the lower half-power frequency, but the same approach is taken to determine the upper half-power frequency. Currently, the inertance correction is left out of the structural wavenumber in an effort to emphasize the process and simple closed form result. Additionally, the drive-point displacement is held constant as a function of frequency. The small parameter δ is determined by satisfying the condition that

$$\mathbb{P}\Big|_{k_{-\delta}} = \frac{1}{2}\mathbb{P}\Big|_{k_M^*} \tag{5.34}$$

which is the definition of the half-power frequency. Referring to Figure 5.7, it is confirmed that the damper value is small compared to the frequency and usually slowly varying with respect to frequency around the resonances. This motivates the assumption that the damper value at the half-power frequency can be approximated with the damper value at resonance. This assumption will be evaluated shortly. The matching condition therefore reduces to

$$\left\langle \bar{V}^2 \right\rangle_x \Big|_{k_{-\delta}} = \frac{1}{2} \left\langle \bar{V}^2 \right\rangle_x \Big|_{k_M^*} \tag{5.35}$$

where the left side is the perturbed spatially averaged mean square velocity and is written as

$$\begin{aligned} \left\langle \bar{V}^2 \right\rangle_x \Big|_{k_{-\delta}} = \frac{((n\pi-\delta)M_1)^2|\beta|^2}{2(n\pi-\delta)} \Bigg(& \frac{2\cos\left((n\pi-\delta)M_1\sin\theta\right)\left[(n\pi-\delta)\cos\left(n\pi-\delta\right)\right]}{\cos\left(2(n\pi-\delta)\right)-\cosh\left(2R\right)} \\ & - \frac{2\cos\left((n\pi-\delta)M_1\sin\theta\right)\sin\left(n\pi-\delta\right)}{\cos\left(2(n\pi-\delta)\right)-\cosh\left(2R\right)} + \frac{\sin\left(2(n\pi-\delta)\right)-2(n\pi-\delta)}{\cos\left(2(n\pi-\delta)\right)-\cosh\left(2R\right)} \Bigg) \end{aligned} \tag{5.36}$$

In order to analytically solve for the small parameter δ that satisfies this condition, the trigonometric functions are rewritten using angle-sum identities [18] and the

small parameter expansions outlined below are applied.

$$\sin\delta \approx \delta, \quad \cos\delta \approx 1 - \tfrac{\delta^2}{2}, \quad \cosh 2R \approx 1 + 2R^2$$

$$\cos\left((n\pi - \delta)M_1 \sin\theta\right) \approx \delta M_1 \sin\theta \sin(k_s^*) + \cos(k_s^*)$$

$$\text{where } k_s^* = n\pi M_1 \sin\theta$$

Applying these expansions allows for the value of the small perturbation δ to be approximated by solving the simple quadratic expression

$$\delta = \frac{-b \pm \sqrt{b^2 - 4ac}}{2a} \tag{5.37}$$

where

$$a = \frac{n\pi}{R^2}\left[(-1)^n\left(R^2+1\right)\cos(k_s^*) - 1\right]$$

$$b = 1 + (-1)^{n+1}\left[2k_s^*\sin(k_s^*) + \cos(k_s^*)\right]$$

$$c = n\pi\left[1 + (-1)^{n+1}\cos(k_s^*)\right]$$

It is important to note that this result confirms that the perturbation required to describe the half-power frequency is dependent on the resonant frequency of interest, the phase difference between drive-points, and the frequency-dependent damper. A quick test confirms that the power peaks are not symmetric and therefore the perturbation parameter calculated for the lower half-power frequency is not as accurate an approximation for the upper frequency. Therefore the same analysis is performed to determine an accurate perturbation for the upper half-power frequency $k_{+\delta}$. The plot in Figure 5.12 shows the location and power at the resonant frequencies and the calculated half-power frequencies and the corresponding powers.

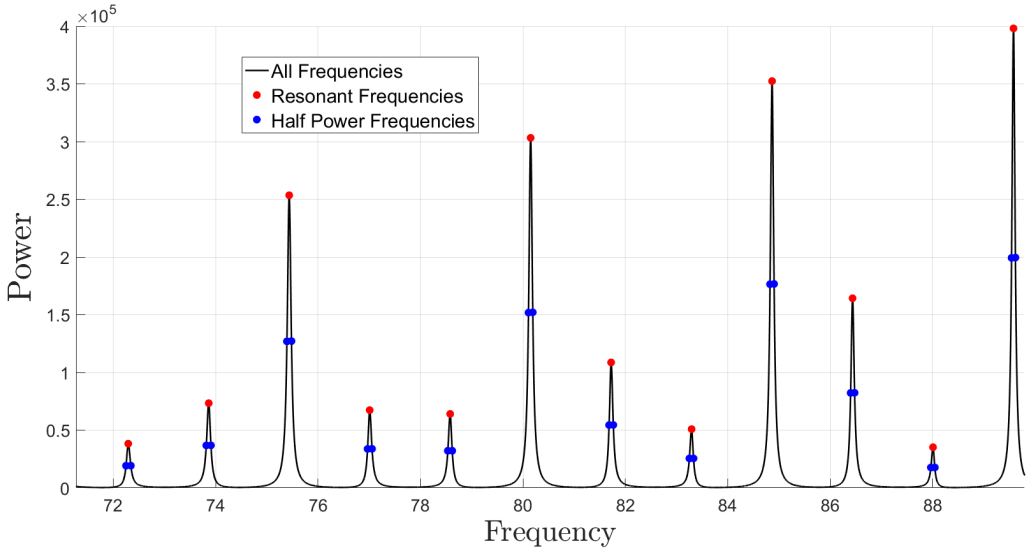

FIGURE 5.12: Estimated power dissipated/radiated at the half-power frequencies and resonant frequencies compared to the calculated power

The power at the half-power frequencies is estimated by the expression

$$\mathbb{P}\Big|_{k_{-\delta}} \approx \frac{2R}{M_1}\left\langle \bar{V}^2 \right\rangle_x \Big|_{k_{-\delta},R=R^*} \tag{5.38}$$

which approximates the damper value with the damper from the corresponding resonance R^*. Figure 5.12 qualitatively confirms that the frequency expansion technique accurately approximates the half-power frequencies with relatively simple closed form expressions. The average percent error between the estimated power at the lower and upper frequencies and half of the power calculated at the resonance is about 0.3% for the current configuration. Although this technique is successful in predicting the half-power frequencies, and therefore the half-power width, it is nonetheless important to confirm the assumption that the damper value at these frequencies can be approximated with the damper value at resonance. In Figure 5.13, the frequency dependent damper determined from the power-matching without the inertance correction is plotted.

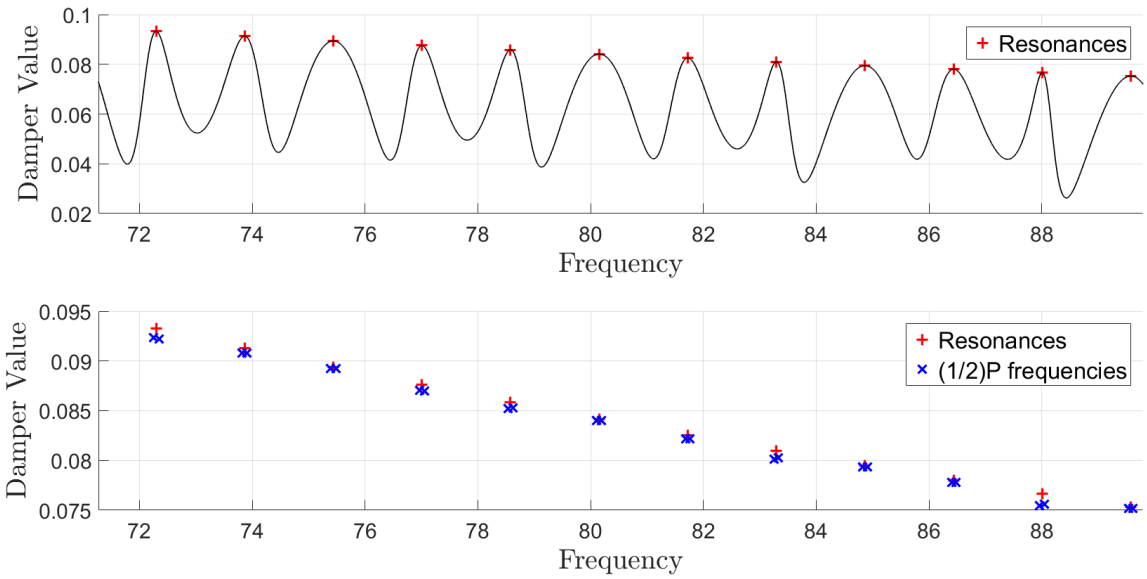

FIGURE 5.13: Damper values at resonance and the calculated half-power frequencies

The calculated damper value at the half-power frequency is denoted with a blue marker, and the value at resonance in red. These markers are almost indistinguishable. It is shown that since the damper is slowly varying with frequency as compared to the perturbation δ, the damper at resonance is an excellent approximation for the damper value at the half-power frequencies. It is interesting to note that the error, however small, in this approximation increases as the resonances experience more destructive interference predicted by Eqn. 5.12 and illustrated by the power amplitude in Figure 5.12. For example, the resonance near $k = 88$ dissipates the least power which suggests its net overall motion is relatively smaller than that at the other resonances and therefore experiences the most interference, and the damper values around this resonance experience the largest gradient within this third-octave band. This observation is important because it portrays a limitation of the current expansion technique; that is, it does not accurately handle resonances that are exactly, or very closely, nulled. However, since these frequencies can be predicted, it is possible to address this condition.

5.5.1 *Effect of Inertance Correction on Damper Value and Power*

The frequency dependent damper values determined from the power-matching analysis with and without the inertance correction are reproduced in Figure 5.14 below for comparison.

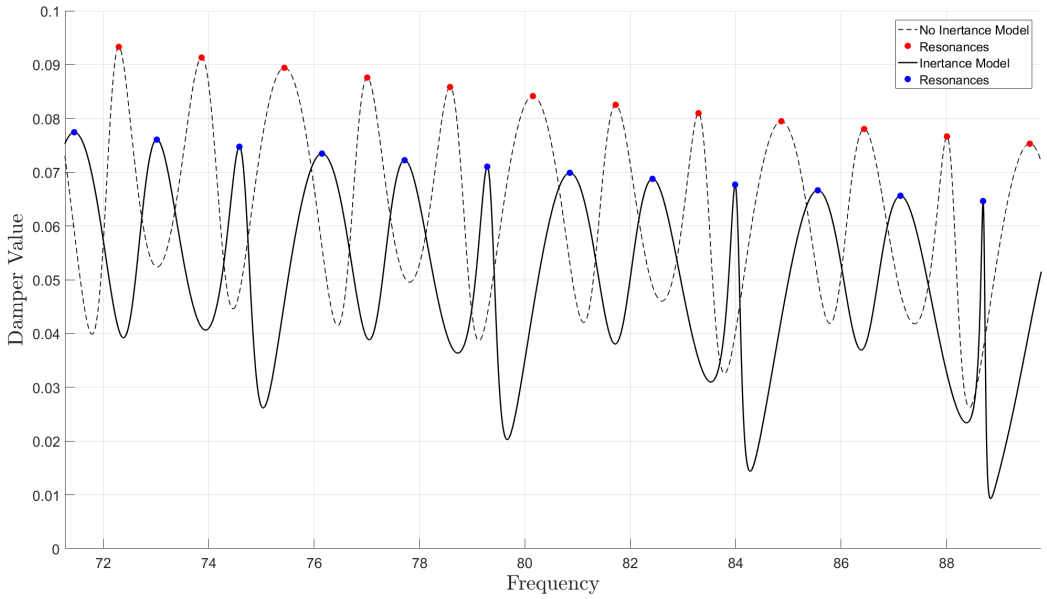

FIGURE 5.14: Comparison of calculated damper value with and without inertance correction

The trend of decreasing damper with increasing frequency is consistent for both models, though the damper determined with the inertance correction is reduced for a given frequency. As expected, the structural resonances of the system are reduced as a result of the additional inertance loading, which is also apparent in Figure 5.15 which compares the power dissipated for both configurations. This reduction in required damper can be explained by interpreting the influence of the inertance as an increase in the "effective" structural Mach number. The in-vacuo Mach numbers are defined as

$$M_1 = \frac{k_1}{k_M}, \quad M_2 = \frac{k_2}{k_M} \tag{5.39}$$

and in essence compare the wave-speed of the structure to the fluid wave speed. However, the inertance correction increases the effective structural wavenumber so that $k_{\chi_1} > k_M$, and so an "effective structural Mach number" $\tilde{M}_1$ and $\tilde{M}_2$ can be defined as

$$\tilde{M}_1 = \frac{k_1}{k_{\chi_1}}, \quad \tilde{M}_2 = \frac{k_2}{k_{\chi_1}} \tag{5.40}$$

so that $\tilde{M} < M$. Increasing the Mach number physically corresponds to an increase in fluid coupling to the membrane motion. This will result in an increase in power radiated through the fluid media and therefore an increase in damper value to match the power dissipated by the suspension. Conversely, a decrease in Mach number would have the opposite effect on damper value. This helps interpret the decreased damper value with the inclusion of the inertance correction as a result of the smaller effective Mach number.

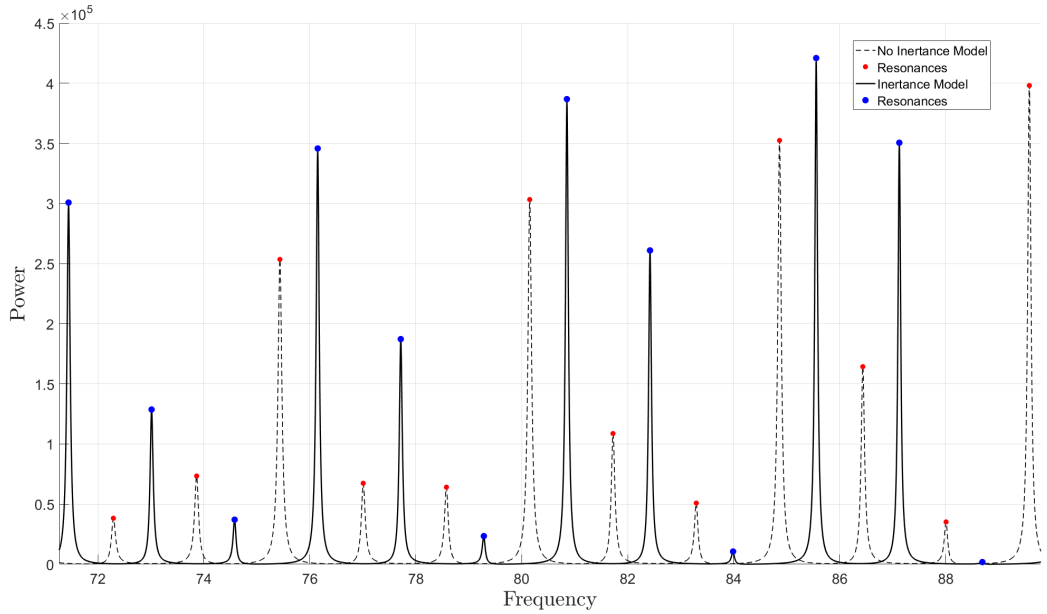

FIGURE 5.15: Comparison of power dissipated with and without the fluid inertance model

6

Comparison of Finite and Infinite Membrane Models

One of the goals for developing a model for a fluid-loaded finite panel is to compare its response to one bay of the periodic structure presented in the first half of this work. The superposition outlined in Figure 5.2 would allow for the comparison of the resultant finite model with the Periodically Fixed Membrane assembled in Chapter 4. However, of particular interest is understanding and describing the redistribution of energy to angles other than the primary angles of reflection and transmission. As previously shown, this redistribution of energy is a result of the reverberation in the structure due to discontinuities, and the influence of the discontinuities are represented by the discretely driven component of both models, presented in Chapter 3 and throughout Chapter 5 for the infinite and finite configurations, respectively. As such, the response of the discretely driven infinite and finite membranes are compared. In these comparisons the motion of the drive-points, and therefore the structural-acoustic response of the systems, are scaled to the Unconstrained Membrane motion in order to begin to develop an understanding of the dynamics of the assembled configurations with the end-points constrained to zero displacement.

6.1 Power Comparison: Damper Suspension vs. Fluid Loading

In Figure 6.1 below, the power dissipated by the finite membrane with the fluid-loading corrections and the power radiated by the infinite Driven Membrane over a third-octave frequency band centered at $k_c = 80$ are presented. These powers are shown as a percent of the power incident on one bay by the incoming oblique acoustic wave. The membrane and fluid parameter values are consistent with those used throughout the development of these models.

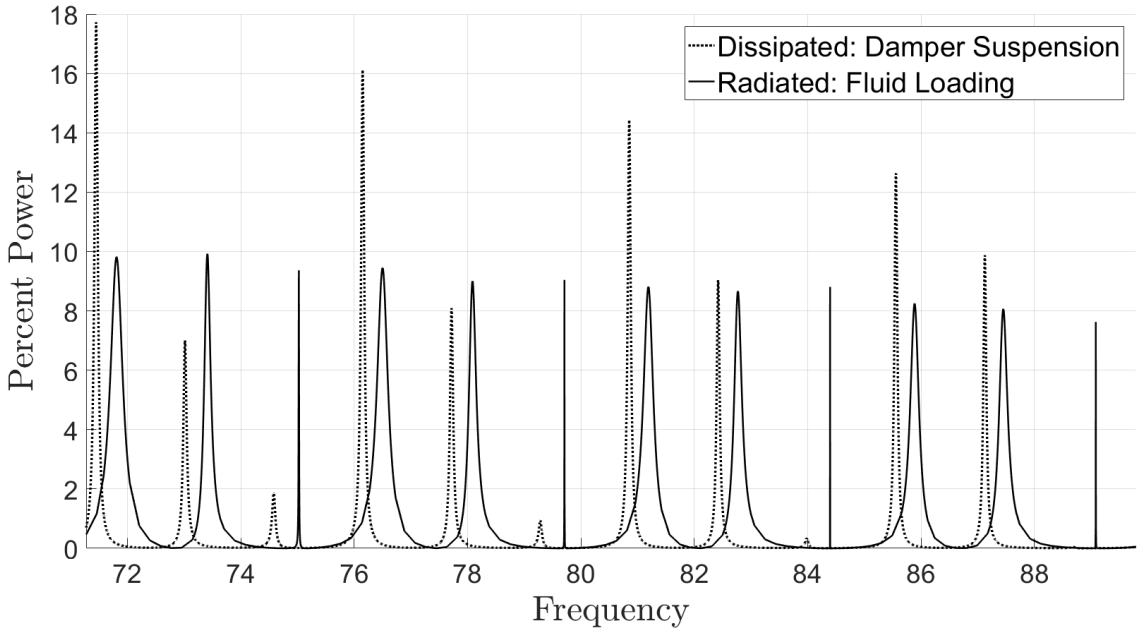

FIGURE 6.1: Comparison of power radiated between the Modified Finite Membrane and the Periodically Driven Membrane

The blue curve in the figure above is identical to the distribution in Figure 4.6 because of the power radiated by the Driven Membrane is equivalent to the total redistribution of energy in the Periodically Fixed Membrane. The black curve describes the power radiated by the modified finite membrane scaled to the Unconstrained Membrane motion at the constraint locations. This distribution, as that for the infinite membrane, shows that the percent power dissipated (or redistributed)

decreases with increasing frequency. This frequency dependence is a result of the decrease in displacement amplitude in the Unconstrained Membrane, which in turn dictates the amplitude of the driven structure motion, and by extension the power amplitude.

The juxtaposition of the two models in Figure 6.1 demonstrates that the modified finite model closely predicts the resonances of the Periodically Fixed Membrane, indicated by the location of the power peaks along the abscissa. Revisiting the convergence of the inertance correction illustrated in Figure 5.3, it is predicted that the next iteration of the inertance solution may result in an improved prediction of the resonant frequencies. The next iteration reduces the modified structural wavenumber relative to first iteration k_{χ_1}, which in turn would result in an increase in the location of the resonant frequencies, thereby shifting the power peaks of the finite model closer to resonances of the infinite fluid-loaded configuration.

Figure 6.1 also shows that one of the short-comings of the current finite model on a viscous suspension is that it does not accurately predict the amplitude of the power radiated by the fluid at the resonances of the infinite model. One of the possible sources of this discrepancy is that the strength of the corresponding damper suspension is determined using a high-frequency approximation to determine the power dissipated/radiated by the finite model. As illustrated in Figure 5.6, there is a perceptible error in applying this model to the frequency band centered at $k_c = 80$, which is the focus of this particular inquiry. Another possible influence that is not considered in the analysis of the finite membrane is that of the adjacent bays of the infinite structure. As a result of the oblique incidence there is a phase difference between the responses of consecutive bays in the infinite structure, which could result in coupling effects not currently addressed by the finite model.

Although the prediction by the finite model of the power amplitude for the infinite Driven Membrane needs to be improved, one of the interesting results of the finite

model is that it appears to predict the relative significance of the infinite Driven Membrane resonances. In Figure 6.1, it is shown that for this case of parameter values, every third resonant power peak of the infinite Driven Membrane is exceedingly sharp with respect to frequency, and the height of every third peak of the finite model is noticeably smaller. The sharpness of the infinite model power peaks appears to correlate with the height of the corresponding power peak from the finite model. As previously concluded, this variation in the efficiency of the resonances is a consequence of the destructive interference of the structural waves resulting from the drive-point phase differences.

6.1.1 Power Comparison: Normal Incidence

In the interest of further corroborating these ideas, the power curves from Figure 6.1 are reproduced for the case of in-phase drive-point motion. This configuration would correspond to the Driven Membrane used to assemble the Periodically Fixed Membrane forced by an acoustic wave at normal incidence, and similarly for the finite model assembly.

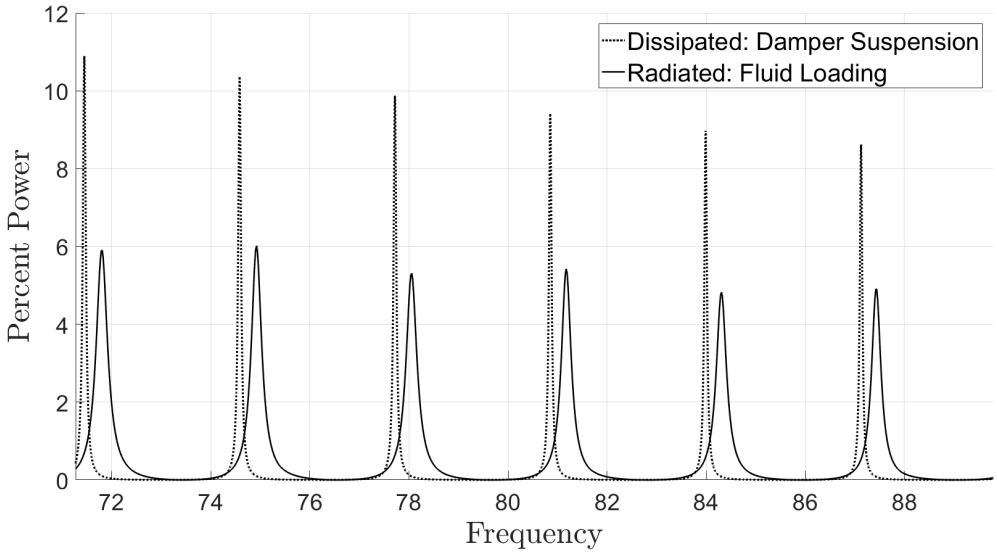

FIGURE 6.2: Comparison of power radiated between the Modified Finite Membrane and the Periodically Driven Membrane for in-phase drive-points

The behaviors in Figure 6.2 agree with the statements made in Section 6.1. The finite model again closely predicts the resonances of the infinite, fluid-loaded, membrane. In Figure 6.2 it is easier to note that the difference in frequency between the resonances of the two structures is approximately constant. The plot of the iterative inertance correction Figure 5.3 shows that the next iteration for the inertance model would equally reduce the structural wavenumber for all frequencies, resulting in a uniform shift to the right of the finite model resonant peaks.

This plot also confirms that there is a noticeable discrepancy in the power amplitude predicted at the resonances by the finite model. However, having eliminated the phase difference between adjacent bays in the infinite model, the difference in power is a consistent overestimate by the finite model as opposed to the variable variation in difference seen in Figure 6.1. This further indicates that the adjacent panels in the infinite model may be affecting the power radiated. Finally, this case of in-phase drive-point motion once again clearly shows that half of the predicted resonant frequencies exactly cancel as a consequences of the destructive interference of the structural waves.

These results indicate that the simple expressions developed for the finite model can be used to predict the number, and relative strength, of the Periodically Fixed Membrane resonances within a frequency band of interest. This is a particularly encouraging result because it suggests that the total scattered power within a frequency band could be predicted by extension of the half-power frequency-expansion analysis applied to the finite model, outlined in Section 5.5.

6.1.2 Periodic Extension of Finite Membrane on a Viscous Suspension

To further understand the similarity and differences between the fluid-loaded Driven Membrane and the finite model with fluid-effect approximations, it is informative to compare their corresponding modal amplitudes. The modal amplitude of the Driven

Membrane is reproduced below from Eqn. 3.33b.

$$\hat{\eta}_{c,m} = \frac{f_o}{(2\pi m)^2 - 4\pi k_1 \sin\theta_i m + (k_1 \sin\theta_i)^2 - k_M^2 \left[1 + \left(\frac{\varepsilon_1}{\sqrt{k_{x,m}^2 - k_1^2}} + \frac{\varepsilon_2}{\sqrt{k_{x,m}^2 - k_2^2}}\right)\right]}$$

It is reasoned that the finite model developed in this Chapter can be periodically extended and consequently treated with modal methods, while carefully addressing the drive-point phase shift as done for the Driven Membrane. This periodic extension does not affect the results of the finite membrane, now represented by a single bay in this extension, because there is no fluid loading to couple the adjacent bays. It does however, allow for the modal amplitudes of the fluid-loaded membrane and the membrane on a suspension to be directly compared. The modal amplitude of the membrane on the viscous suspension, with the first iteration of the inertance correction, is

$$\hat{\eta}_{R,m} = \frac{f_o}{(2\pi m)^2 - 4\pi k_1 \sin\theta_i m + (k_1 \sin\theta_i)^2 - k_M^2 \left[1 + \left(\frac{\varepsilon_1}{\sqrt{k_M^2 - k_1^2}} + \frac{\varepsilon_2}{\sqrt{k_M^2 - k_2^2}}\right) + ik_1\bar{R}\right]}$$

and its eigenfunctions are the same as those for the Driven Membrane (Eqn. 3.33a). Generating the expressions for these modal amplitudes allows for direct comparison of the dissipative mechanism of both systems, denoted by the last terms of the respective denominators. For the fluid loading case, the resistive effect is a function of ε_1 and ε_2, and for the membrane on a suspension the resistive effects are proportional to the damper strength. These expressions indicate that the dissipative effects on the fluid-loaded structure are only active for the radiating modes, yet the dissipative effect of the viscous suspension is constant for all modes. Thus, all of the mode shapes of the membrane on a suspension contribute to the power dissipated, as opposed to a finite number of modes in the case of the fluid-loaded configuration.

7

Conclusions

7.1 Analytical Numerical Matching and Ongoing Efforts

The method of Analytical Numerical Matching has been shown to efficiently treat the high resolution content near structural discontinuities by describing this slowly converging region using an analytical description, while the overall motion of the structure is described using traditional modal methods. ANM is particularly powerful in treating scattering of structures with discontinuities because the overall motion of the structure is inversely proportionally to the slowly converging influence of the discontinuity, which ANM is designed to efficiently model.

This ANM analysis has allowed for an efficient description of the reflection and transmission of membranes forced by oblique acoustic waves, with reduced computational costs as compared to traditional modal methods. This thesis presents the intensity redistribution for the case of a single incident planar wave at a fixed frequency and incidence angle. Expanding this analysis to describe broadband, random incidence forcing to the structure will facilitate the implementation of this work to energy-intensity methods for describing room acoustics, such as the Energy-Intensity

Boundary Element Method (EIBEM) developed at Duke University [19], [20], [17], [21].

With the object of improving the EIBEM by developing relationships that formalize the coupling between energy flow in the acoustic and structural systems realized at the boundaries of enclosures, more realistic structures should be investigated. The use of a membrane is a first-order model for flexible boundaries that provides valuable insight into the effect that the dynamics of barriers with structural discontinuities has on the reflected and transmitted acoustic fields. However, improving this model to include the structural properties and wave behavior of plates and shells will provide more realistic directivity patterns for the resulting acoustic fields of adjacent enclosures. The ANM method can be expanded to carefully treat various types of discontinuities in these structures by extending the Local Solution constraints to higher order derivatives of the structure dynamics.

The results from this, and future work are expected to provide considerable physical insight into the behavior of acoustic fields in coupled enclosures with flexible boundaries, particularly the mechanisms producing spatial variation in the sound field. This will allow for improved efficiency and robustness in designing acoustic spaces.

7.2 Finite Structure Model and Ongoing Efforts

The viscous suspension and inertance correction used to approximate the effects of the fluid loading on the finite membrane were insightful models, particularly in predicting the number of resonances in a frequency band as well as their relative efficiencies as radiators. It was demonstrated that the viscous damping model can be used to predict the total energy radiated by the finite structure. An analytical approximation of the half-power widths at the resonances can be used to estimate the total power radiated within a frequency band, and the simple closed form results

from the Rayleigh Integral can be used to predict the acoustic intensity directivity.

The error associated with the power predicted by this model and the comparison of the corresponding modal displacement amplitudes indicate that alternative resistive paradigms should be considered. The analogy of these modal amplitudes suggested that limiting the effect of the damper on the finite model to the mode shapes that correspond to radiation may improve the agreement between the Driven Membrane and Forced-Forced Membrane with fluid effect corrections. In conjunction with the insight on the role that edge effects have on radiation from subsonic structures [16], this analysis motivates a different damping arrangement. The conclusions from Bliss' work proves that the high frequency radiation from sub-critical finite panels is independent of the structure length, and therefore inspires a model that concentrates the dissipative effects at the end-points of the in-vacuo finite membrane. Nevertheless, when extending this work to supersonic membranes, it may be determined that the distributed damping framework is an appropriate model because the entire length of the structure becomes a radiator [17].

References

[1] R. Loftman and D. Bliss, "The application of analytical/numerical matching to structural discontinuities in structural/acoustic problems," *J. Acoust. Soc. Am.*, vol. 101, no. 2, pp. 925–935, February 1997.

[2] F. Fahy, *Sound and Structural Vibration: Radiation, Transmission and Response*. Academic Press Inc, 1985.

[3] T. R. Quackenbush and D. B. Bliss, "Free wake calculation of rotor flow fields for interactional aerodynamics," *Vertica*, vol. 14, pp. 313–327, 1990.

[4] D. B. Bliss and W. O. Miller, "Efficient free wake calculations using analytical/numerical matching," *J. Am. Helicopter Soc*, vol. 38, pp. 870–879, 1993.

[5] T. R. Quackenbush, C.-M. G. Lam, and D. B. Bliss, "Vortex methods for computational analysis of rotor/body interaction," *J. Am. Helicopter Soc*, vol. 39, pp. 14–24, 1994.

[6] R. Loftman and D. Bliss, "Scattering from fluid-loaded cylindrical shell with periodic circumferential constraints using analytical/numerical matching," *J. Acoust. Soc. Am.*, vol. 106, no. 3, pp. 1271–1283, 1999.

[7] P. Morse and K. Ingard, *Theoretical Acoustics*. McGraw-Hill",

[8] L. E. Kinsler, A. R. Frey, A. B. Coppens, and J. V. Sanders, *Fundamentals of Acoustics*. Hoboken, NJ: John Wiley & Sons, Inc, 1993.

[9] D. T. Blackstock, *Fundamentals of Physical Acoustics*. John Wiley & Sons,Inc, 2000.

[10] A. D. Pierce, *Acoustics: An Introduction to Its Physical Principles and Applications*. Acoustical Society of America, 1989.

[11] K. Graff, *Wave Motion in Elastic Solids*. Dover Publications, INC, 1975.

[12] M. C. Junger and D. Feit, *Sound, Structures, and Their Interaction*. The MIT Press, 1982.

[13] J. O. Smith, *Spectral Audio Signal Processing*. `http://ccrma.stanford.edu/~jos/sasp/`, accessed 2016, online book, 2011 edition.

[14] M. Villa and D. Bliss, "Reflection and transmission by an elastic barrier with periodic discontinuities forced by oblique acoustic waves." 5th Joint Meeting of the Acoustical Society of America and the Acoustical Society of Japan. Honolulu, HI, 2016.

[15] R. Haberman, *Applied Partial Differential Equations*. Pearson, 2013.

[16] D. Bliss, "Radiation from vibrating panels at high frequency including an inquiry into the role of edges and drive points." 4th Joint Meeting of the Acoustical Society of America and the Acoustical Society of Japan. Honolulu, HI, 2006.

[17] D. Bliss, L. Franzoni, K. Michalis, and J. Rouse, "Energy-intensity boundary element method for predicting of sound fields in enclosures including radiation from vibrating boundaries." Noise and Vibration: Emerging Methods. Keynote Speaker, 2009.

[18] M. Spiegel, S. Lipschutz, and J. Liu, *Mathematical Handbook of Formulas and Tables*. McGraw Hill, 2009.

[19] L. Franzoni, D. Bliss, and J. Rouse, "An acoustic boundary element method based on energy and intensity variables for prediction of high-frequency broadband sound fields," *J. Acoust. Soc. Am.*, vol. 110, no. 6, pp. 3071–3080, December 2001.

[20] J. W. Rouse, "An acoustic boundary element method using time-averaged variables for predicting broadband high frequency fields," Ph.D. dissertation, Duke University, Durham, NC, 2004.

[21] K. Michalis, "Modeling specular and diffuse reflection sound fields in enclosures with an energy-intensity boundary element method," Ph.D. dissertation, Duke University, Durham, NC, 2011.